

See discussions, stats, and author profiles for this publication at: <https://www.researchgate.net/publication/231631936>

# Ultrafast Electron Diffraction and Structural Dynamics: Transient Intermediates in the Elimination Reaction of C<sub>2</sub>F<sub>4</sub>I<sub>2</sub>

ARTICLE *in* THE JOURNAL OF PHYSICAL CHEMISTRY A · APRIL 2002

Impact Factor: 2.69 · DOI: 10.1021/jp014144r

---

CITATIONS

37

---

READS

26

5 AUTHORS, INCLUDING:



Hyotcherl Ihee

Korea Advanced Institute of Science and Tec...

128 PUBLICATIONS 3,235 CITATIONS

SEE PROFILE



Boyd M Goodson

Southern Illinois University Carbondale

64 PUBLICATIONS 1,526 CITATIONS

SEE PROFILE

# Ultrafast Electron Diffraction and Structural Dynamics: Transient Intermediates in the Elimination Reaction of C<sub>2</sub>F<sub>4</sub>I<sub>2</sub>

Hyotcherl Ihee, Boyd M. Goodson, Ramesh Srinivasan, Vladimir A. Lobastov, and Ahmed H. Zewail\*

Laboratory for Molecular Sciences, Arthur Amos Noyes Laboratory of Chemical Physics, California Institute of Technology, Pasadena, California 91125

Received: November 12, 2001; In Final Form: February 25, 2002

We give a full account of our earlier report on the structural dynamics in the elimination reaction of C<sub>2</sub>F<sub>4</sub>I<sub>2</sub>, as studied with the newly constructed third-generation apparatus for ultrafast electron diffraction (UED3) at Caltech (Ihee, H.; Lobastov, V. A.; Gomez, U.; Goodson B. M.; Srinivasan, R.; Ruan, C.-Y.; Zewail, A. H. *Science* **2000**, 291, 458). Improvements in experimental stability, sensitivity, resolution, and versatility provided by UED3 permitted the reaction to be probed with spatial and temporal resolution of  $\sim 1$  ps and  $\sim 0.01$  Å, respectively, and with a sensitivity to chemical change of  $\sim 1\%$ . In addition to the improvements in apparatus design, a number of advancements in data processing, analysis, and modeling were developed which are described here in detail for the first time. With UED, we directly observed the prompt (within 5 ps) formation of the C<sub>2</sub>F<sub>4</sub>I transient structure, and its subsequent decay with a rate of  $(25 \pm 7 \text{ ps})^{-1}$ . The molecular structure of the C<sub>2</sub>F<sub>4</sub>I radical was determined to be classical, not bridged—and was refined via a least-squares fitting procedure. These experimental results are compared with recent predictions obtained from ab initio and density functional theory calculations (Ihee, H.; Kua, J.; Goddard, W. A.; Zewail A. H. *J. Phys. Chem. A* **2001**, 105, 3623), yielding quantitative agreement to within 0.03 Å between the experimental and theoretical structures for the transient intermediate.

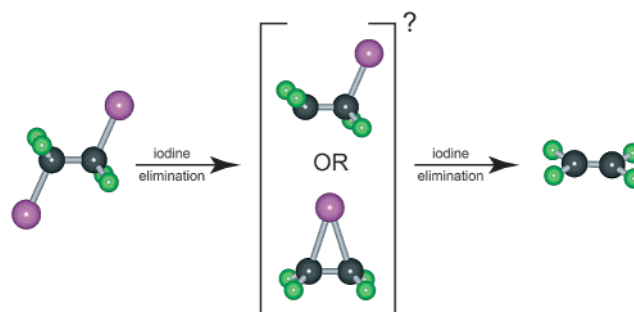
## I. Introduction

Ultrafast electron diffraction (UED)<sup>1–9</sup> now approaches the combined spatial and temporal resolution necessary for tracking all nuclear coordinates, thereby permitting the direct observation of molecular structural dynamics in real time. Several challenges to the advancement of UED have been surmounted with numerous improvements in the overall design of the apparatus. In addition, the diffraction-difference method—which employs the pixel-by-pixel subtraction of a reference (ground-state) diffraction signal from the signals recorded over the course of the reaction—can be used to select the contributions resulting only from structural changes of the species under study, thereby enhancing the sensitivity of UED to chemical change.

In this contribution, the utility of our approach is demonstrated with the first application of our third-generation UED apparatus, UED3:<sup>4</sup> a study of the structural dynamics in the elimination of iodine from 1,2-diiodotetrafluoroethane (C<sub>2</sub>F<sub>4</sub>I<sub>2</sub>) to form tetrafluoroethylene (C<sub>2</sub>F<sub>4</sub>) on the picosecond time scale, and the direct determination of the molecular structure of the short-lived C<sub>2</sub>F<sub>4</sub>I radical intermediate—we determined it to be classical, not bridged, in nature. The relevant structures for this reaction are shown below in Scheme 1. Here, we provide a full account of the study, with details of the observation and analysis. We also compare the structure of the intermediate observed by UED with the findings obtained by ab initio and density functional theory calculations.

The elimination reaction of C<sub>2</sub>F<sub>4</sub>I<sub>2</sub> is a prototypical reaction in ultrafast spectroscopic studies of photoinitiated reactions.<sup>10,11</sup> The consecutive (nonconcerted) nature of the C–I bond breakage was elucidated via picosecond photofragment spectroscopy.<sup>10</sup> Following UV excitation, a biexponential formation

SCHEME 1



of atomic iodine was observed—with a prompt component ( $\leq 1$  ps) and a much slower second component ( $\sim 30$ – $150$  ps, depending on the total excitation energy)—indicating a two-step process with a weakly bound radical intermediate (C<sub>2</sub>F<sub>4</sub>I). The femtochemistry of C<sub>2</sub>F<sub>4</sub>I<sub>2</sub> was subsequently investigated using femtosecond kinetic-energy resolved time-of-flight (KETOF) mass spectrometry, permitting the state, velocity, and angular evolution of the relevant species to be resolved.<sup>11</sup> Femtosecond UV excitation (at 277 nm) causes the rapid ( $\sim 200$  fs) loss of the first iodine atom, the first C–I bond breakage, and the formation of the transient C<sub>2</sub>F<sub>4</sub>I radical intermediate—with the kinetic energy distributions of the fragments directly measured. The remaining internal energy, left to redistribute within the vibrational degrees of freedom of the C<sub>2</sub>F<sub>4</sub>I radicals, was enough to induce secondary C–I fragmentation in a majority of the hot intermediates—resulting in the loss of the second iodine atom and the formation of the tetrafluoroethylene product in  $\sim 25$  ps.

The chemistry of halogen elimination reactions is of general interest because products are usually formed under stereochem-

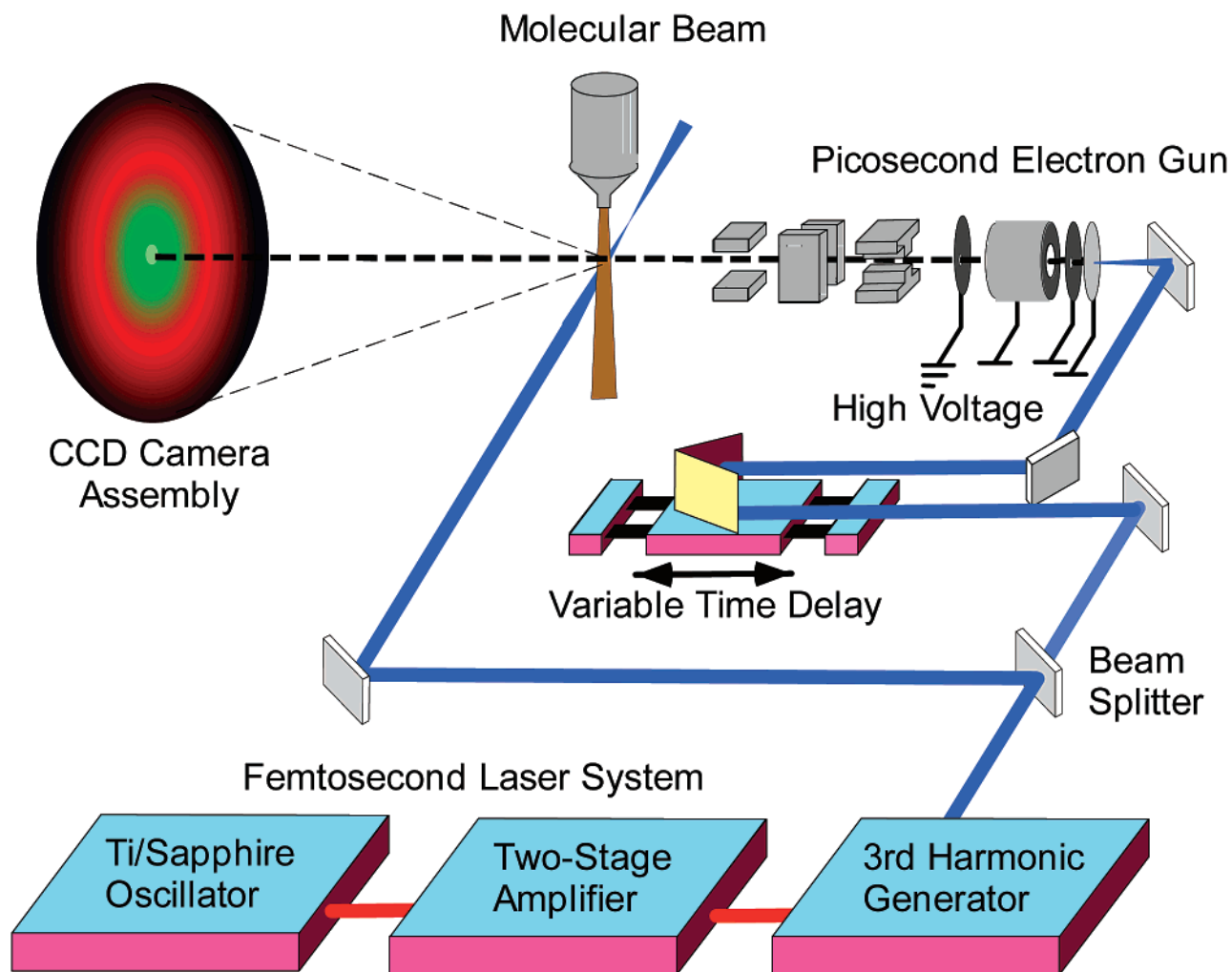


**Figure 1.** Schematic representation of key components of the UED apparatus.<sup>4</sup> Details of our third-generation device will be presented elsewhere.<sup>20</sup>

ical control with respect to the final positions of the functional groups about the newly formed double bond.<sup>12–15</sup> The origin of this well-known behavior has been hypothesized to lie in the geometry of the intermediate species of the reaction. For example, previous quantum chemical calculations<sup>16</sup> have shown that  $\text{CH}_2\text{BrCH}_2$  and  $\text{CH}_2\text{ICH}_2$  radicals should form stable, symmetrically “bridged” structures, consistent with the Skell hypothesis for the origin of stereochemical control in such systems.<sup>17–19</sup> In a symmetrically bridged structure, the primary halide (i.e., I or Br) is shared equally between the two  $-\text{CR}_2$  moieties, whereas in a “classical” structure, the primary halide would reside predominantly on one  $-\text{CR}_2$  moiety.<sup>19</sup> A bridged structure would prevent rotation about the C–C bond, thereby maintaining the functional group positions in the final product. However, the substitution of hydrogens with highly electronegative fluorines can cause dramatic changes in molecular structure (and reactivity). For example, it is well-known that the  $\text{CF}_3$  radical is highly nonplanar, whereas  $\text{CH}_3$  is planar, and the  $\text{C}_2\text{F}_4\text{I}$  radical structure may be much different from that of  $\text{C}_2\text{H}_4\text{I}$ .

Although the presence of  $\text{CF}_2\text{XCF}_2$  radicals can be readily detected in photodissociation reactions of  $\text{CF}_2\text{XCF}_2\text{X}$  molecules via spectroscopy, UED offers the means to track all of the nuclear coordinates over the course of a chemical reaction, allowing the *molecular structures* of these radicals to be observed directly. Thus, the elimination reaction of  $\text{C}_2\text{F}_4\text{I}_2$  is an ideal process to study with UED: (1) it affords the opportunity to observe the structural dynamics of a prototypical

nonconcerted reaction involving the loss of two highly scattering heavy atoms (providing a strong diffraction difference signal), and (2) it permits the determination of the molecular structure of a transient radical intermediate that belongs to an important family of chemical reactions.

The remainder of this contribution is organized as follows. Section II describes the experimental methods used to obtain the UED images. Section III describes the data analysis employed in our UED experiments (details of the 2-D image processing procedure can be found in the Appendix). Section IV contains a comprehensive discussion of the results and analysis for the  $\text{C}_2\text{F}_4\text{I}_2$  data. This discussion includes: a comparison of ground-state  $\text{C}_2\text{F}_4\text{I}_2$  diffraction data with previous conventional diffraction experiments; the structural dynamics of the nonconcerted iodine elimination reaction; and the molecular structure determination of the  $\text{C}_2\text{F}_4\text{I}$  radical intermediate. Section V concludes with a summary of the present work.

## II. Experimental Section

UED data were obtained with our third-generation apparatus, which will be described in greater detail in a separate publication by Lobastov et al.<sup>20</sup> A schematic drawing is presented in Figure 1. Briefly, the UED apparatus is composed of an amplified femtosecond laser system (Spectra Physics), an electron gun, a high-vacuum scattering chamber, a molecular beam, a 2-D imaging system, and a time-of-flight mass spectrometer for the

identification of molecular species. Amplified femtosecond laser pulses provided by a Ti:Sapphire laser system (3 mJ,  $\sim 120$  fs, 800 nm) are frequency-tripled with a third-harmonic generator to give UV fs pulses (350  $\mu$ J, 267 nm). An optical beam splitter is used to direct part of this UV output into the scattering chamber to initiate the chemical reaction, whereas a smaller fraction of the laser power is first directed into a delay line with a computer-controlled translation stage, and then focused onto a back-illuminated silver photocathode to generate electron pulses via the photoelectric effect. High intensity, picosecond electron bursts at 30 keV (de Broglie wavelength 0.067 Å) are produced by the home-built electron gun, which features magnetic focusing, electrostatic deflection, and built-in streaking capabilities for in situ measurement of the electron pulse width. The laser provides a 1 kHz repetition rate for the electron pulses, which were  $\sim 4$  ps in duration in these experiments and contained  $\sim 25$  000 electrons per pulse.

The sample was delivered into the scattering chamber as a molecular beam from an effusive-jet expansion source with a  $\sim 125$   $\mu$ m nozzle. The temperature of the sample storage bulb, the gas inlet manifold, and the sample nozzle was monitored and controlled independently. The laser pulses, the electron pulses, and the molecular beam intersected in a mutually perpendicular arrangement just below the sample nozzle. The interaction region, dictated by the overlap of the laser, electron, and molecular beam waists, was typically  $400 \pm 50$   $\mu$ m. Electron diffraction patterns were recorded with a low-noise 2-D CCD camera assembly capable of single-electron detection; the detector assembly principally comprises a phosphor scintillator (P-47), an image intensifier (Hamamatsu), and finally the CCD camera (Photometrics, KAF-1000). Because the scattering intensity in electron diffraction decays rapidly with increasing scattering angle (usually varying over 6–8 orders of magnitude), a radially symmetric, variable neutral-density apodizing optical filter was coated onto the backside of the scintillator. This filter allows the simultaneous measurement of diffracted intensities varying over 7 orders of magnitude, thereby effectively extending the dynamic range of detected intensities and consequently improving the precision of internuclear distance measurements in comparison with previous generations of UED.

The reaction zero-of-time was determined by the ion-induced lensing technique.<sup>21</sup> In this approach, a calibration gas (e.g., CF<sub>3</sub>I) is delivered to the scattering chamber via the sample nozzle; the spatial profile of the undiffracted electron beam is then monitored while the arrival time of the electron pulses is varied with respect to that of the laser pulses. Figure 2 shows a typical photoionization-induced lensing transient. When the electron and laser pulses coincide within the interaction region, the focused laser induces multiphoton ionization in the gas molecules, leading to charge separation and the formation of an electric field gradient. This field gradient effects a corresponding increase in the ellipticity of the undiffracted electron beam. The time at which the ellipticity of the electron beam begins to deviate from that of a symmetric profile is defined to be the reaction zero-of-time. The overall temporal resolution of the experiment, about 5 ps, includes contributions from the electron pulse width, the laser pulse width, and the group-velocity mismatch<sup>20,22</sup> ( $\sim 3$  ps) between light and electron pulses.

Samples of C<sub>2</sub>F<sub>4</sub>I<sub>2</sub> (Lancaster, 98%) were used without further purification, but were degassed with several freeze–pump–thaw cycles and stabilized with copper filings. High-purity xenon (Spectra Gases, 99.999%) was used as an atomic reference gas (see discussion below), and the CF<sub>3</sub>I gas (99%) used for determining the zero-of-time in the lensing experiments was

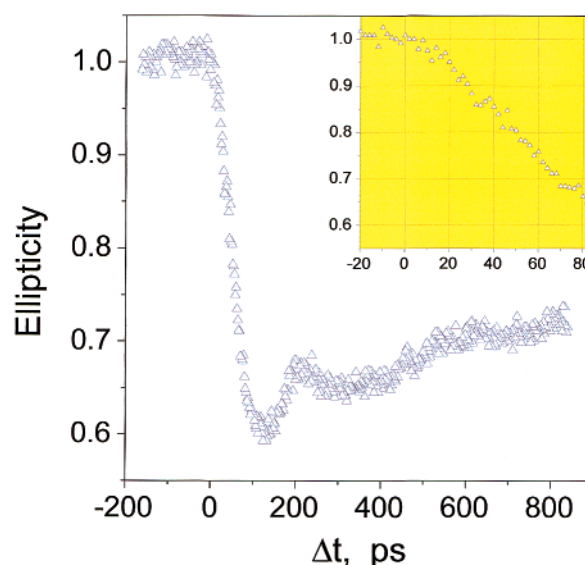


**Figure 2.** Direct determination of time zero from the rise in ellipticity of electron beam. Experimental photoionization-induced lensing transient for a molecular beam of CF<sub>3</sub>I. The ellipticity is defined as the ratio of vertical and horizontal e-beam widths (fwhm) on the screen. The insert shows an expanded view from  $-20$  ps to  $80$  ps.

purchased from Aldrich. To maintain satisfactory sample pressure at the needle (estimated to be a few Torr), the sample bulb, gas manifold, and nozzle temperatures were respectively maintained at 60 °C, 100 °C, and 120 °C for the C<sub>2</sub>F<sub>4</sub>I<sub>2</sub> experiments. The background pressure of the scattering chamber was typically  $\sim 2 \times 10^{-4}$  Torr during the experiment.

### III. Data Analysis

**A. Basic Theory of Gas-Phase Electron Diffraction.** The general theory of gas-phase electron diffraction is well-established (see for example, ref 23); this section summarizes the basic formulas used in the analysis of conventional scattering patterns and the subsequent extraction of internuclear separations. Electron scattering intensity is typically expressed as a function of  $s$ , the magnitude of momentum transfer between an incident electron and an elastically scattered electron

$$s = \frac{4\pi}{\lambda} \sin\left(\frac{\theta}{2}\right) \quad (1)$$

where  $\lambda$  is the de Broglie wavelength of the electrons (0.067 Å at 30 keV), and  $\theta$  is the scattering angle.

The total scattering intensity,  $I$ , is a sum of contributions from individual atoms (atomic scattering,  $I_A$ ) superimposed with interference terms from all atom–atom pairs (molecular scattering,  $I_M$ )

$$I(s) = I_A(s) + I_M(s) \quad (2)$$

If it is assumed that the electronic potentials of each atom in the molecule are independent (the independent atom model), the atomic scattering intensity may be written as a sum of elastic and inelastic scattering contributions

$$I_A(s) = C \sum_{i=1}^N \left( |f_i(s)|^2 + 4 \frac{S_i(s)}{a_0^2 s^4} \right) \quad (3)$$

where  $N$  is the number of atoms in the molecule,  $f_i$  and  $S_i$  are the elastic and inelastic scattering amplitudes for atom  $i$ ,  $a_0$  is the Bohr radius, and  $C$  is a proportionality constant. The



contributions from spin-flip scattering amplitudes ( $g_i$ ) have not been included as they are generally neglected for high-energy electron diffraction experiments.<sup>24</sup>

For the purpose of structural determination, only  $I_M$  is of interest because it contains the information regarding inter-nuclear separations. The molecular scattering intensity of an isotropic sample can be written as a double sum over all  $N$  atoms in the molecule

$$I_M(s) = C \sum_i^N \sum_{j \neq i}^N |f_i| |f_j| \exp\left(-\frac{1}{2} l_{ij}^2 s^2\right) \cos(\eta_i - \eta_j) \frac{\sin(sr_{ij})}{sr_{ij}} \quad (4)$$

where  $f_i$  is the elastic scattering amplitude for the  $i$ th atom,  $\eta_i$  is the corresponding phase term,  $r_{ij}$  is the internuclear separation between atoms  $i$  and  $j$ ,  $l_{ij}$  is the corresponding mean amplitude of vibration, and  $C$  is a proportionality constant. The scattering factors  $f$  and  $\eta$  depend on  $\lambda$ ,  $s$ , and atomic number  $Z$ ; tables of  $f$  and  $\eta$  are available in the literature.<sup>25,26</sup> The relative contribution of each atomic pair to the total molecular scattering intensity is roughly proportional to  $(Z_i Z_j)/r_{ij}$ . Because  $I_M(s)$  decays approximately with  $s^5$ , the modified molecular scattering intensity,  $sM(s)$ , is often used instead of  $I_M(s)$  in order to highlight the oscillatory behavior (instead of the sinc function) of the diffraction signal at higher values of  $s$  (see ref 23); note that the  $\sim s^{-5}$  dependence arises from the  $s^{-2}$  contribution from  $f_i$  and similarly from  $f_j$ , along with the  $1/s$  term of the sinc function. The modified molecular scattering intensity can be defined either as

$$sM(s) = s \frac{I_M(s)}{I_A(s)} \quad (5a)$$

or

$$sM(s) = s \frac{I_M(s)}{|f_a| |f_b|} \quad (5b)$$

where  $a$  and  $b$  correspond to two chosen atoms in the molecule (usually atoms with relatively high  $Z$ ). In our current analysis, eq 5a was used (unless indicated otherwise).

The corresponding radial distribution curve,  $f(r)$ , may be derived from  $sM(s)$  via a Fourier (sine) transform

$$f(r) = \int_0^{s_{\max}} sM(s) \sin(sr) \exp(-ks^2) ds \quad (6)$$

where the damping constant  $k$  accounts for the finite  $s$  range of the detector. In our experiments, the available experimental scattering intensity,  $sM^E(s)$ , typically ranged from  $s_{\min} = 1.5 \text{ \AA}^{-1}$  to  $s_{\max} = 18.5 \text{ \AA}^{-1}$ . For the range from 0 to  $s_{\min}$ , the theoretical scattering intensity,  $sM^T(s)$ , is appended to avoid distortions of the radial distribution baseline (note that all data analyses and structural refinements were performed on  $sM^E(s)$  curves prior to this step). Correction for nonnuclear scattering was included so as to express the radial distribution curve as a sum of Gaussian functions, with each peak representing a given internuclear separation in the molecule.<sup>27</sup> Although all structural information is contained in the molecular scattering function, the radial distribution curve is more intuitive for qualitative interpretation because it directly reflects the relative density of internuclear distances in the molecule.

**B. Analysis of 1-D Diffraction Data: Ground-State Structures.** The procedure for processing our diffraction data

is illustrated in Figure 3; details of the generation of 1-D diffraction curves from the 2-D images obtained with the CCD camera are given in the Appendix. The experimental diffraction intensity curve is a sum of the desired structural information,  $I_M^E(s)$ , and a background intensity profile,  $I_B^E(s)$

$$I^E(s) = I_B^E(s) + I_M^E(s) \quad (7)$$

where  $I_B^E(s)$  contains contributions from atomic scattering,  $I_A(s)$ , and the experimental background response. Thus, from eq 5 the modified experimental molecular scattering intensity is given by

$$sM^E(s) = s \frac{I^E(s) - I_B^E(s)}{I_A(s)} \quad (8a)$$

or

$$sM^E(s) = s \frac{I^E(s) - I_B^E(s)}{|f_a| |f_b|} \quad (8b)$$

We did not obtain the curve for  $I_B^E(s)$  by merely calibrating the detector because the amount of scattered laser light and other factors varied from experiment to experiment and with each molecular system. Instead, background curves were independently estimated for each experiment. Such background curves may be ascertained using different methods, three of which are described: (1) A crude yet often effective approximation is a low-order polynomial curve fit through all the data points of  $I^E(s)$ ; (2) A more rigorous way of obtaining  $I_B^E(s)$  exploits the sinusoidal nature of  $I_M(s)$ , cycling above and below zero several times over the experimental detection range. This approach introduces a set of zero-positions,  $s_n$ , of  $s$  where the theoretical molecular intensity curve,  $I_M^T(s)$ , crosses zero: i.e.,  $I_M^T(s_n) = 0$ . If  $I_M^T(s)$  approaches  $I_M^E(s)$ , it should then hold from eq 7 that  $I^E(s_n) = I_B^E(s_n)$  at the zero-positions,  $s_n$ . Therefore,  $I_B^E(s)$  can be approximated by fitting a polynomial curve through  $[s_n, I^E(s_n)]$  (for example, see later in Figure 6(c)); (3) A third way to estimate  $I_B^E(s)$  is to express  $I_B^E(s)$  independently as a polynomial curve defined by the variable coefficients of each order, and to optimize these variables by minimizing the difference (more precisely,  $\chi^2$ ) between  $I_M^T(s)$  and  $I_M^E(s)$ . This method should produce the same background curve obtained with the second method if there is no systematic error. These three methods can also be applied to the time-resolved diffraction data, as explained later.

**C. Time-Resolved Experiments: The Diffraction-Difference Method.** To follow the structural changes that occur over the course of a given chemical reaction, we recorded a series of averaged 2-D diffraction images with varying time delay,  $t$ , between the pump (laser) and probe (electron) pulses. Each of these images thus reflects the transient behavior of the molecular structures at the corresponding temporal delay following laser excitation. Unlike the ground-state data, the scattering intensity at a time  $t > 0$ ,  $I(t > 0; s)$ , contains contributions from more than one type of molecular species—not just the parent molecules, but also intermediates and products of the reaction. Therefore, the time-resolved scattering intensity  $I(t; s)$  can be written as a sum of the individual scattering intensities from each species at time  $t$ ,  $I_\alpha(t; s)$

$$I(t; s) = \sum_\alpha I_\alpha(t; s) \quad (9)$$

where  $\alpha$  indexes all possible structures occurring over the course

## Ground State Structural Analysis

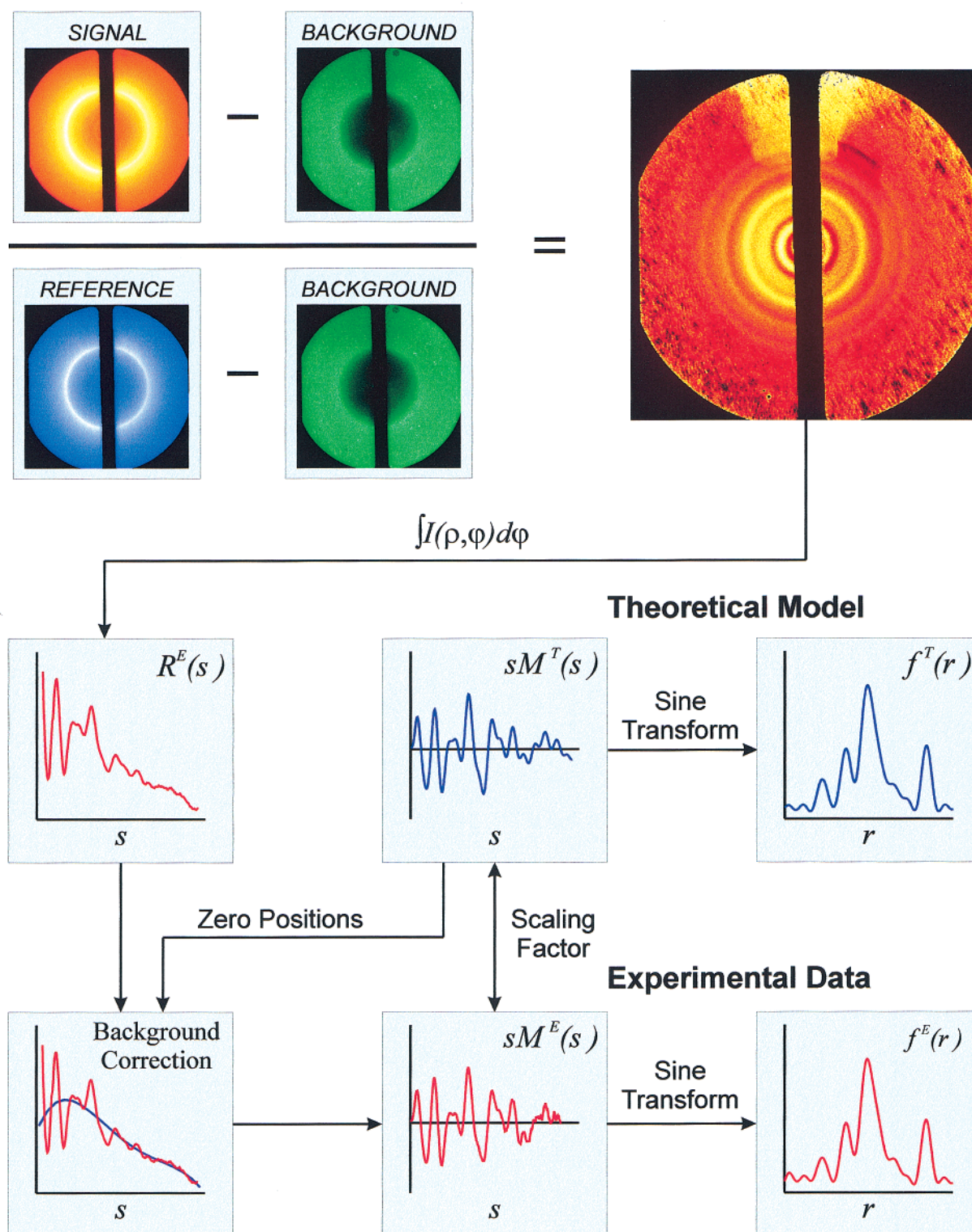


**Figure 3.** Schematic of the processing procedure for 2-D diffraction images and ground-state data analysis (see also the Appendix). Subtraction of the background image and division by the reference gas image yields a 2-D "ratio" image that clearly shows the rings of the molecular scattering signal. Following radial averaging of the ratio image, the unwanted background signal is subtracted from the 1-D curve to give the desired  $sM(s)$  curve, which can be compared with theoretical curves generated with iteratively refined structural parameters describing a given molecular species; the corresponding  $f(r)$  curves are obtained via sine transform.

of the reaction. If the molecular structures of the species formed (transient or otherwise) do not change significantly over the

time window that defines the species  $\alpha$ , we may partition the time dependence of  $I_\alpha(t; s)$  into the relative concentration of



## Time-Resolved Structural Analysis

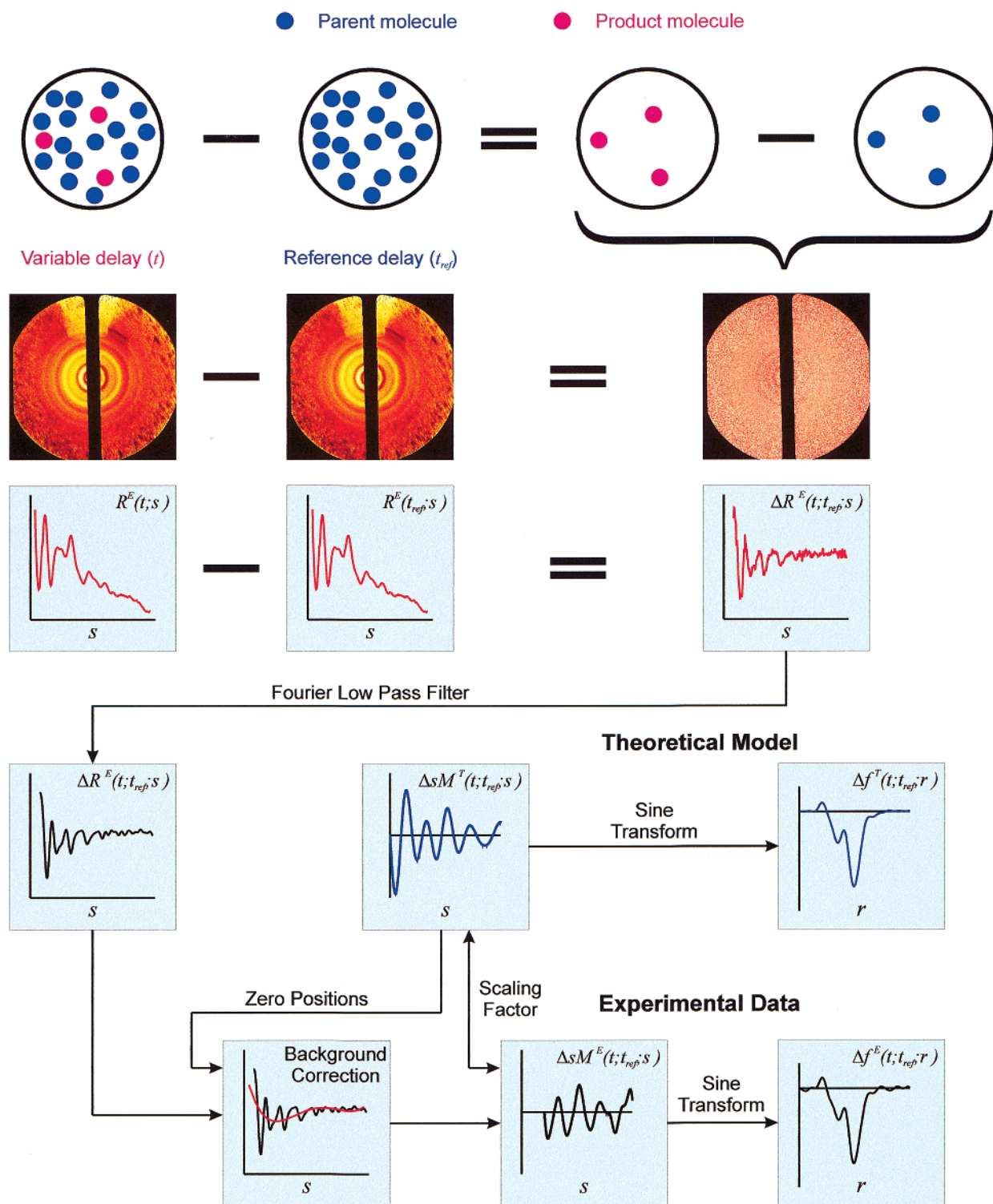


**Figure 4.** Schematic of the diffraction-difference analysis procedure for time-resolved experiments. The diffraction-difference method employs the direct, pixel-by-pixel subtraction of a reference diffraction signal (obtained at a negative time) from the diffraction signal obtained at a positive time. The resulting difference signal reflects only contributions from structural changes within the molecules. After Fourier filtering and background subtraction, information regarding the changing structures can be obtained from the experimental  $\Delta sM(s)$  curves; as before,  $\Delta f(r)$  curves are obtained via sine transform.

structure  $\alpha$  by writing

$$I(t, s) = \sum_{\alpha} I_{\alpha}(t, s) \approx \sum_{\alpha} p_{\alpha}(t) \cdot I_{\alpha}(s) \quad (10)$$

where  $p_{\alpha}(t)$  is the population (or mole fraction) of a given

structure  $\alpha$  and  $I_{\alpha}(s)$  is the time independent scattering intensity from that structure. In the present case, we will consider  $\alpha$  to refer to parent, intermediate, and product structures.

In UED, all species present will scatter the incident electrons regardless of their participation in the chemical reaction. Thus,

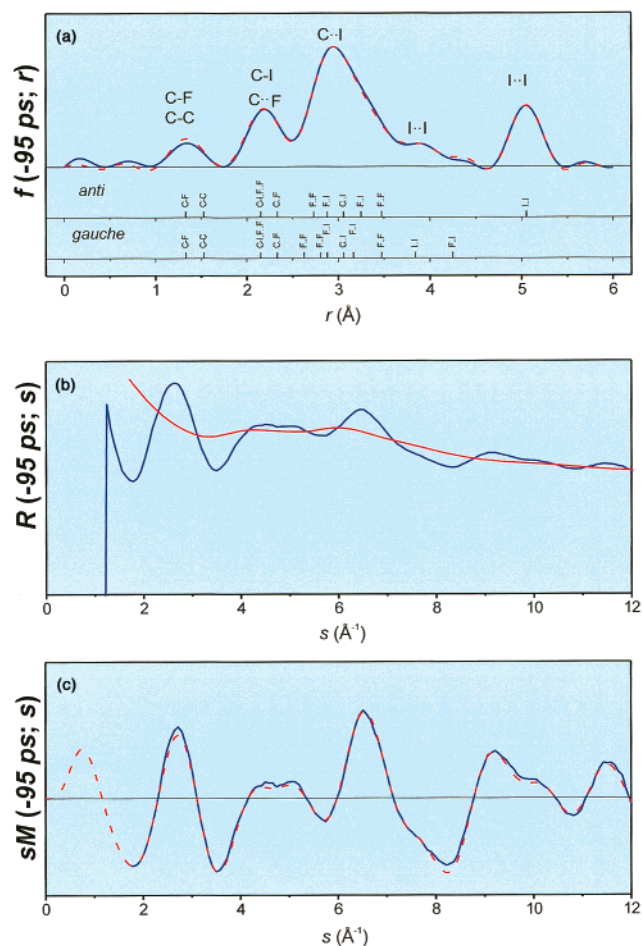


**Figure 5.** Ground-state structure of  $\text{C}_2\text{F}_4\text{I}_2$ . (a) Comparison of corresponding theoretical (red) and experimental (blue)  $f(r)$  curves obtained at  $-95$  ps following sine transformation of the  $sM(s)$  curves in (c) according to eq 6. The major interatomic distances for the anti and gauche  $\text{C}_2\text{F}_4\text{I}_2$  structures obtained by Hedberg and co-workers<sup>31</sup> are indicated for comparison. (b) Raw electron diffraction data (blue curve) obtained at  $-95$  ps, following division by the atomic reference signal and radial summation of the 2-D data. The smooth background is shown as a red curve. (c) Comparison of theoretical (red) and experimental (blue)  $sM(s)$  curves for the data in (b) following refinement of the relative fractions of the anti and gauche structures.

in most cases, the vast majority ( $>85$ – $90\%$ ) of the diffracting media is comprised of nonreacting parent molecules:  $p_{\text{parent}} \gg p_{\text{intermediate}}$  or  $p_{\text{product}}$ . Furthermore, the molecular scattering intensity from a reaction fragment is usually weaker than that from a parent molecule because it has fewer internuclear pairs. Therefore, to accentuate the diffraction signal arising from structural changes occurring over the course of the reaction, we employed the so-called diffraction-difference method (illustrated in Figure 4), whereby we use a reference image to obtain the diffraction-difference signal,  $\Delta I(t; t_{\text{ref}}; s)$ , from the relation

$$\Delta I(t; t_{\text{ref}}; s) = I(t; s) - I(t_{\text{ref}}; s) \quad (11)$$

where  $t_{\text{ref}}$  refers to the reference time (e.g., prior to the arrival of the reaction-initiating laser pulse). Combining eqs 10 and 11 gives

$$\Delta I(t; t_{\text{ref}}; s) \approx \sum_{\alpha} p_{\alpha}(t) \cdot I_{\alpha}(s) - \sum_{\alpha} p_{\alpha}(t_{\text{ref}}) \cdot I_{\alpha}(s) = \sum_{\alpha} \Delta p_{\alpha}(t; t_{\text{ref}}) \cdot I_{\alpha}(s) \quad (12)$$

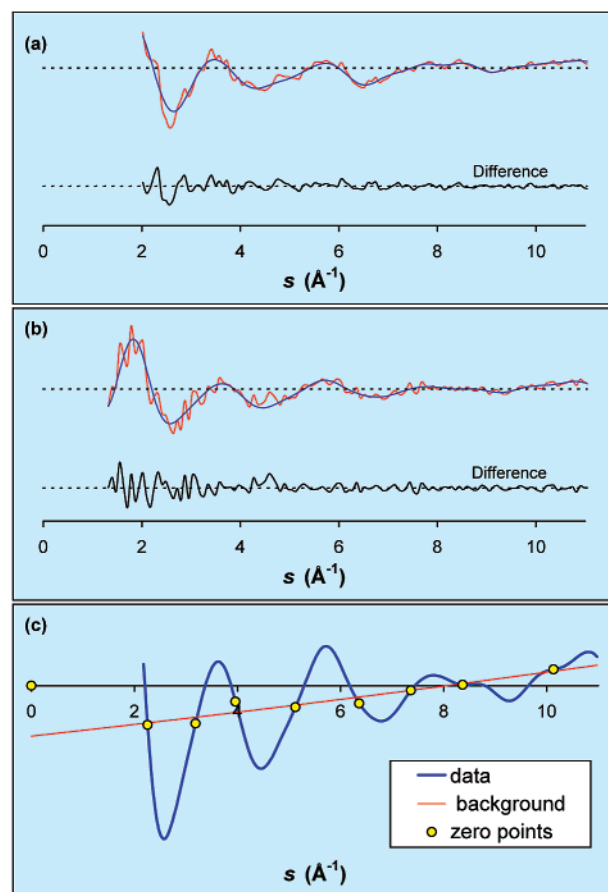


**Figure 6.** (a,b) Effect of Fourier filtering on 1-D raw diffraction-difference curves. The raw data is shown in red, and the Fourier filtered data (obtained with a  $\sim 8.7$ - $\text{\AA}$  low-pass filter) is shown in blue. The difference between the raw and filtered data shows the noise removed by the filter. (a)  $\Delta R^E(405 \text{ ps}; -95 \text{ ps}; s)$ . (b)  $\Delta R^E(\infty \text{ ps}; 5 \text{ ps}; s)$ . (c) Background fitting through the zero-crossing points of the experimental  $\Delta R^E(\infty; 5 \text{ ps}; s)$  data. The experimental  $\Delta R^E(\infty; 5 \text{ ps}; s)$  is shown in blue, and the background  $\Delta R^E_{\text{B}}(\infty; 5 \text{ ps}; s)$  obtained by fitting a low-order polynomial through the zero-crossing points (yellow circles) is shown in red.

Equation 12 thus presents  $\Delta I(t; t_{\text{ref}}; s)$  in terms of the *changing populations* of the molecular structures involved—if the molecular structure of a given species *does* undergo significant structural change during the time window of the experiment, then it may be necessary to refine its structural parameters at each point in time.

The diffraction-difference method has several general advantages. First, the large (unwanted) background signal from atomic scattering is a common contribution to all images—regardless of the temporal delay and the nature of the reaction—and can, therefore, be essentially removed by the subtraction. It follows from the definition of the total scattering intensity,  $I^E (= I_{\text{M}}^E + I_{\text{B}}^E)$ , that the experimental difference curve is given by

$$\Delta I^E(t; t_{\text{ref}}; s) = \Delta I_{\text{M}}^E(t; t_{\text{ref}}; s) + \Delta I_{\text{B}}^E(t; t_{\text{ref}}; s) \quad (13)$$

Because  $I_{\text{B}}^E$  is composed mostly of atomic scattering, which is unchanged over the course of a chemical reaction,  $\Delta I_{\text{B}}^E(t; t_{\text{ref}}; s)$  should be nearly zero. Thus, whereas the total diffraction signal,  $I(t; s)$ , is dominated by the background intensity,  $I_{\text{B}}^E(t; s)$ , the diffraction-difference curve is dominated by the molecular scattering intensity,  $I_{\text{M}}^E(t; s)$



$$\Delta I^E(t; t_{\text{ref}}; s) \approx \Delta I_M^E(t; t_{\text{ref}}; s) \quad (14)$$

Second, any intrinsic systematic error of the detection system will be greatly reduced (or effectively eliminated) by the subtraction. Third, each diffraction-difference curve reflects comparable contributions from the parent and product structures—in contrast to the original raw data, wherein only a relatively small fraction of the signal comes from products (and/or intermediates), with the vast majority of the signal originating from the parent. Therefore, the significance of the product contribution is dramatically enhanced in  $\Delta I(t; t_{\text{ref}}; s)$ :  $|\Delta p_{\text{parent}}| \approx |\Delta p_{\text{intermediate}}| \approx |\Delta p_{\text{product}}|$  (Note that the diffraction-difference method does not depend on the specific formulas used to express  $I_M$ . In this study, the classical description, eq 4, is used. Formulas more sophisticated than eq 4 can be used if required, and the diffraction-difference approach would still be valid and useful).

If desired, knowledge of the fractional changes of the species involved in the reaction,  $\Delta p_{\alpha}(t; t_{\text{ref}})$ , can be used to extract the molecular diffraction signal resulting only from the reaction's products. The parent diffraction signal ( $I_{\text{parent}}(s)$ , obtained at a negative time) is scaled by  $\Delta p_{\text{parent}}(t; t_{\text{ref}})$  and added to the diffraction difference signals obtained at positive times, thereby canceling out the parent contribution (see eq 12)

$$\Delta I(t; t_{\text{ref}}; s) - \Delta p_{\text{parent}}(t; t_{\text{ref}}) \cdot I_{\text{parent}}(s) = \sum_{\alpha \neq \text{parent}} \Delta p_{\alpha}(t; t_{\text{ref}}) \cdot I_{\alpha}(s) \quad (15)$$

(Note that  $\Delta p_{\alpha}(t; t_{\text{ref}})$  is typically a negative number). This procedure,<sup>28</sup> which we have referred to as the “product-isolated” or “product-only” method, has been utilized frequently in our more recent work.<sup>8,9</sup>

Prior to analyzing the diffraction-difference signals, high-frequency noise was reduced with low-pass Fourier filtering (performed via convolution with a parabolic cutoff function valued 1.0 at 0.0 Å and 0.0 at ~8.7 Å). This filter, which was carefully chosen to prevent any significant damping of higher-frequency components of the diffraction signal, reduced the standard deviation values resulting from least-squares fitting by about half compared to similar analyses of unfiltered data but did not significantly alter the results of the fits. An example of this filtering is presented in Figure 6.

**D. Least-Squares Fitting.** Refinements of the diffraction data were performed with software developed in-house using a procedure (similar to that used in conventional gas-phase electron diffraction<sup>29</sup>) that iteratively minimizes the statistical  $\chi^2$ . For example, for a given difference curve,  $\Delta I^E(t; t_{\text{ref}}; s)$ , the determination of the relative fractions or structural parameters of each molecular species was made by minimizing

$$\chi^2 = \sum_{s_{\text{min}}}^{s_{\text{max}}} \frac{[S_c \cdot \Delta sM^T(t; t_{\text{ref}}; s) - \Delta sM^E(t; t_{\text{ref}}; s)]^2}{[\sigma(s)]^2} \quad (16)$$

where the  $\Delta sM(s)$  is the difference modified molecular scattering intensity,  $\sigma(s)$  is the standard deviation of  $\Delta sM^E(t; t_{\text{ref}}; s)$  at each  $s$  position (over the available range), and  $S_c$  is a scaling factor (whose magnitude is determined by the amplitude of the ground-state signal).  $\Delta sM^E(t; t_{\text{ref}}; s)$  is obtained from  $\Delta I^E(t; t_{\text{ref}}; s)$  through eq 8, and the  $\sigma(s)$  values are calculated from the corresponding values of  $\sigma(\text{pix})$  (the standard deviation of the scattering intensity at each pixel radius; see Appendix)<sup>28</sup> with appropriate error propagation.<sup>30</sup>

Beginning with an assumed initial product distribution and the starting structural parameters for each species, the software

first fits the residual background,  $\Delta I_B^E(t; t_{\text{ref}}; s)$ , with the experimental  $\Delta I^E(t; t_{\text{ref}}; s)$  values at the zero-positions ( $s_n$ ) of the theoretical  $\Delta I_M^T(t; t_{\text{ref}}; s)$  curve. Then the experimental  $\Delta sM^E(t; t_{\text{ref}}; s)$  curve is obtained with the background-free  $\Delta I$  through eq 8, and  $\chi^2$  is calculated to evaluate the quality of the fit. This procedure is repeated until the best least-squares fit between theoretical and experimental  $\Delta sM(s)$  curves is reached (i.e., until  $\chi^2$  is minimized). In the fitting algorithm, the absolute amplitude of the diffraction-difference signal may then be scaled to that of the ground-state signal to give the relative number densities of every structure at each time delay over the course of the experiment.

## IV. Results and Discussion

**A. Ground-State Structures of C<sub>2</sub>F<sub>4</sub>I<sub>2</sub>.** The experimental results concerning the ground-state structures of C<sub>2</sub>F<sub>4</sub>I<sub>2</sub> are shown in Figure 5. To observe the ground-state structures, we time the electron pulse to arrive before the initiation pulse (i.e., at a negative time). Figure 5(a) shows the radial distribution curve obtained for C<sub>2</sub>F<sub>4</sub>I<sub>2</sub>,  $f(-95 \text{ ps}; r)$ , obtained from the  $-95 \text{ ps}$  data; Figure 5(b) shows the 1-D raw diffraction data,  $R^E(-95 \text{ ps}; s)$ , (following division by the Xe scattering intensity), and the corresponding  $R_B^E(-95 \text{ ps}; s)$  baseline curve (here, the “ $R$ ” refers to the fact that the data reflects a “ratio” of the scattering data from the sample and the xenon reference gas—see Appendix). Following subtraction of the  $R_B^E(-95 \text{ ps}; s)$  baseline, the corresponding  $sM^E(-95 \text{ ps}; s)$  curve was generated according to eq 8 and is shown as the blue curve in Figure 5(c). The experimental data was then compared to a diffraction curve generated from structural parameters obtained by conventional electron diffraction.<sup>31</sup>

The C<sub>2</sub>F<sub>4</sub>I<sub>2</sub> molecule is known to have two conformational minima with respect to torsional rotation about the C–C bond: an anti structure with a  $\angle \text{ICCI}$  torsion angle of  $180^\circ$  and  $C_{2h}$  symmetry, and a gauche structure with  $\angle \text{ICCI} \approx 70^\circ$  and  $C_2$  symmetry. In the study by Hedberg and co-workers, the experimental structural parameters for C<sub>2</sub>F<sub>4</sub>I<sub>2</sub> were refined under the simplifying assumption that the anti and gauche conformers possess identical values for the structural parameters, except for the  $\angle \text{ICCI}$  dihedral angle. Correspondingly, identical *anti/gauche* parameter values were used in our analysis, although recent quantum chemical calculations have suggested that the C–C and C–F distances of the anti conformers may be slightly shorter, and the C–I distances slightly longer, than those of the gauche conformers.<sup>32</sup>

Both ground-state structures were observed in the electron diffraction data shown in Figure 5; the ratio of these conformers was determined via least-squares refinement to be  $76:24 \pm 2$  anti:gauche. This ratio, which is governed by the sample temperature and the energy difference between the conformers, was identical to the previous results obtained by Hedberg and co-workers at  $120^\circ \text{C}$ .<sup>31</sup> The theoretical  $sM^T(-95 \text{ ps}; s)$  curve, obtained from the refinement of the conformer ratio, is shown as the red curve in Figure 5(b). Excellent agreement can be seen between  $sM^E(-95 \text{ ps}; s)$  and  $sM^T(-95 \text{ ps}; s)$ , and in the corresponding experimental and theoretical  $f(-95 \text{ ps}; r)$  curves shown in Figure 5(a).

The various interatomic distances present in the anti and gauche C<sub>2</sub>F<sub>4</sub>I<sub>2</sub> structures are indicated at the bottom of Figure 5(a), and can be summarized as follows: the peak at  $\sim 1.4 \text{ Å}$  results from covalent C–F and C–C distances; the peak at  $\sim 2.2 \text{ Å}$  results from covalent C–I and nonbonded F...F and C...F distances; the broad peak at  $\sim 3 \text{ Å}$  comprises nonbonded F...I, C...I, and F...F distances; and the peaks at  $\sim 3.8 \text{ Å}$  and  $\sim 5.1$

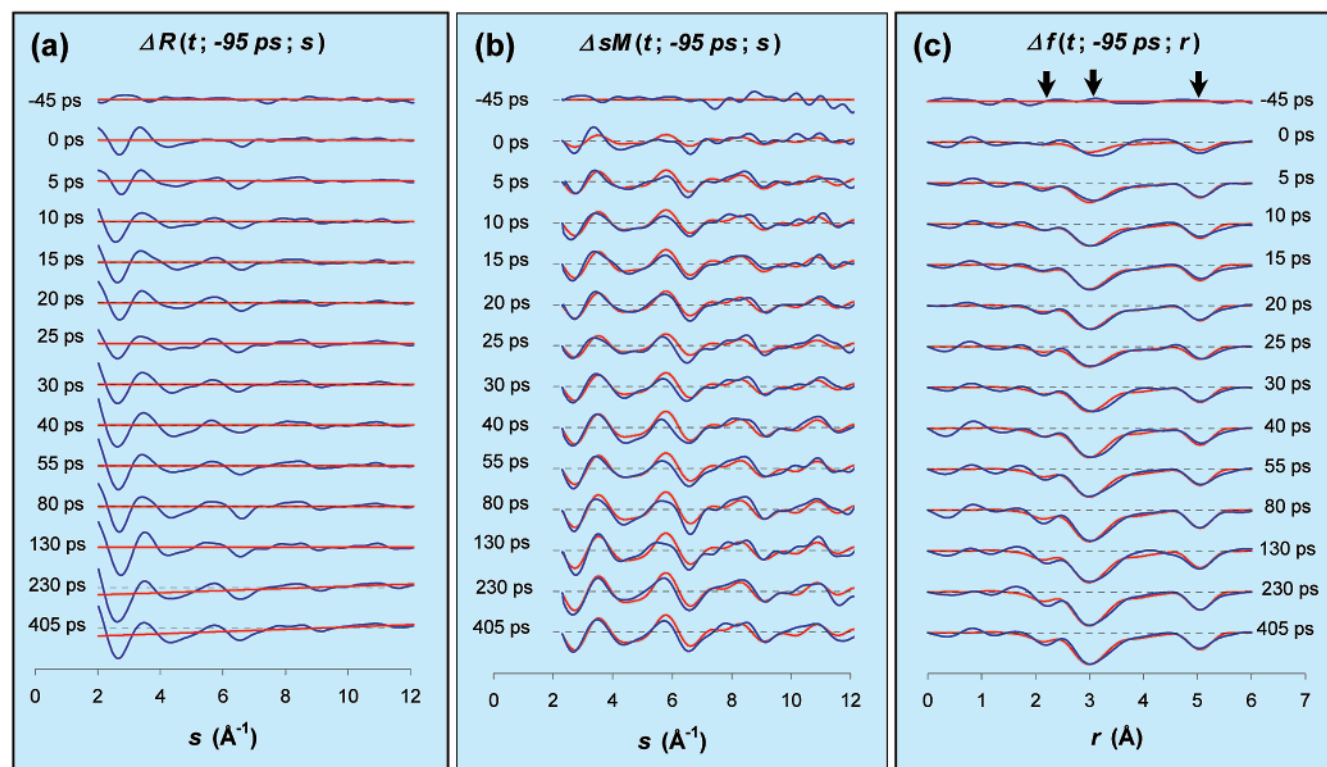


**Figure 7.** Time-resolved structural changes from the elimination of iodine from  $\text{C}_2\text{F}_4\text{I}_2$ . (a) Raw diffraction-difference signals,  $\Delta R(t; -95 \text{ ps}; s)$ , (blue curves), shown with the baseline curves (red). (b) Experimental (blue) and theoretical (red)  $\Delta sM(t; -95 \text{ ps}; s)$  curves obtained at varying time delays. (c) Corresponding experimental (blue) and theoretical (red)  $\Delta f(t; -95 \text{ ps}; r)$  curves. Major peaks are highlighted with arrows.

$\text{\AA}$  respectively correspond to the nonbonded  $\text{I}\cdots\text{I}$  distances for the gauche and anti conformers.

**B. Structural Dynamics of the  $\text{C}_2\text{F}_4\text{I}_2$  Reaction.** UED images were acquired for the elimination reaction of  $\text{C}_2\text{F}_4\text{I}_2$  over a range of time delays ( $t$ ) from  $-95 \text{ ps}$  to  $+405 \text{ ps}$ . The data at  $-95 \text{ ps}$  served as a reference representing the signal contributed only by parent molecules. A set of diffraction-difference curves with  $t_{\text{ref}} = -95 \text{ ps}$  was obtained from the images using the procedures described in section III and the Appendix. Figure 6(a) shows the effects of the Fourier filter on a raw diffraction-difference curve,  $\Delta R^E(405 \text{ ps}; -95 \text{ ps}; s)$ , whereas Figure 7(a) shows the entire set of difference curves,  $\Delta R^E(t; -95 \text{ ps}; s)$ , and the corresponding residual background curves,  $\Delta R_B^E(t; -95 \text{ ps}; s)$ . No change is observed in the  $t = -45 \text{ ps}$  data as the electron pulses probe the molecules prior to the initiation of the chemical reaction. At  $t = 0 \text{ ps}$ , a periodic pattern instantaneously appears (within our time resolution), resulting from structural changes in the molecules. The difference signal becomes more pronounced with increasing time.

The corresponding  $\Delta sM^E(t; -95 \text{ ps}; s)$  curves, created in part by subtraction of the baseline curves obtained for each time delay, are shown in Figure 7(b). The difference procedure removes most of the systematic background signal, resulting in a small, nearly linear background curve for the raw difference curves in Figure 7(a). Finally, the corresponding time-dependent difference radial distribution curves,  $\Delta f^E(t; -95 \text{ ps}; r)$ , which directly indicate the structural changes occurring over the course of the reaction, are shown in Figure 7(c). It is significant to note that the negative peak intensity at  $\sim 5.1 \text{ \AA}$  in the  $\Delta f(r)$  curves remains constant after  $5 \text{ ps}$ , whereas the peak intensities around  $2\sim 3 \text{ \AA}$  continue to increase over a longer time scale.

As shown in the figure, the negative peak at  $\sim 5.1 \text{ \AA}$  results from the loss of the  $\text{I}\cdots\text{I}$  internuclear separation of the anti conformer of the parent  $\text{C}_2\text{F}_4\text{I}_2$  molecules, while those at  $2\sim 3$

$\text{\AA}$  result primarily from the depletion of  $\text{C}\cdots\text{I}$ ,  $\text{F}\cdots\text{I}$ , and  $\text{C}\cdots\text{I}$  distances. These observations demonstrate the nonconcerted nature of the structural changes in the reaction: The first step ( $\text{C}_2\text{F}_4\text{I}_2 \rightarrow \text{C}_2\text{F}_4\text{I} + \text{I}$ ) is essentially complete within our  $\sim 5 \text{ ps}$  resolution—consistent with the  $\sim 200 \text{ fs}$  time constant measured previously in this laboratory,<sup>11</sup> whereas the second step ( $\text{C}_2\text{F}_4\text{I} \rightarrow \text{C}_2\text{F}_4 + \text{I}$ ) is considerably slower, taking place over tens of picoseconds.

Theoretical  $\Delta sM^T(t; -95 \text{ ps}; s)$  and  $\Delta f^T(t; -95 \text{ ps}; s)$  curves (red curves in Fig 7(b) and 7(c)) were obtained by refining the relative fractions of the species present against the corresponding experimental  $\Delta sM^E(t; -95 \text{ ps}; s)$  curve (blue) at each time delay. These refinements were performed as follows. The depletion of the  $\text{C}_2\text{F}_4\text{I}_2$  parent molecules was fit using the structural parameters determined by Hedberg and co-workers, and with the anti:gauche conformer ratio held fixed at the 74:26 value determined above; the latter practice assumes that there is no disproportional selectivity in the depletion of anti vs gauche  $\text{C}_2\text{F}_4\text{I}_2$  conformers during the loss of the first iodine atom (i.e., that the  $\text{C}\cdots\text{I}$  chromophores of the anti and gauche conformers have identical absorption cross sections and reactivity).

Starting structures for the  $\text{C}_2\text{F}_4\text{I}$  radical intermediate were constructed using the structural parameters provided by recent quantum chemical calculations.<sup>32</sup> Although one goal of our studies was to experimentally determine the structure of this transient species (the subject of section IV D), the calculations suggested that the structure of this species is nonbridged in nature, with anti and gauche conformers qualitatively similar to the parent structures. Nevertheless, we initially included a bridged  $\text{C}_2\text{F}_4\text{I}$  structure in our early fraction refinements; doing so, however, had a detrimental effect on the overall fits—and typically resulted in negative values for the bridged fraction. Therefore, our final fraction refinements of the  $\Delta sM(t; -95 \text{ ps};$

s) data included only the nonbridged, “classical” anti and gauche  $C_2F_4I$  structures.

The high internal energy of the  $C_2F_4I$  radical following laser excitation was included in our analysis. After each parent molecule absorbs a UV photon (107 kcal/mol) and fragments into  $C_2F_4I + I$ , 48 kcal/mol are available for the internal energy of the  $C_2F_4I$  radical and the translational motion of both fragments (for the I channel, whereas only 26 kcal/mol is left over after the formation of  $I^*$ , spin excited iodine); 59 kcal/mol of the incident energy is required to break the first C–I bond (in addition to the 22 kcal/mol needed to match the spin–orbit energy of  $I^*$ ). According to previous experiments from this group,<sup>11</sup> about 67% (for the I channel; 59% for  $I^*$  channel) of the energy is partitioned into the translational degrees of freedom, whereas the remaining 33% [for the I channel (16 kcal/mol); 41% for the  $I^*$  channel (11 kcal/mol)] goes into the internal energy of the  $C_2F_4I$  radical. Accounting for the branching ratio of 30:70 for the I and  $I^*$  channels<sup>11</sup> yields 12.5 kcal/mol for the available internal energy acquired in the  $C_2F_4I$  radical. However, because some of the available thermal energy from the parent molecule at 393 K ( $\sim 6.7$  kcal/mol) remains in  $C_2F_4I$ , the total available internal energy is about 19 kcal/mol. If complete thermalization of the internal degrees of freedom is assumed, a vibrational temperature of  $\sim 800$  K can be estimated for the  $C_2F_4I$  radical (based on the total remaining internal energy and quantum chemical predictions for the vibrational frequencies<sup>32</sup>). Although the use of thermalized structures proved adequate for the present study, we note that in general, complete thermalization may not always be a good approximation—particularly for UED studies of complex molecules at high internal energies.<sup>8</sup>

Using theoretical values for the rotational barrier separating anti and gauche structures,<sup>32</sup> microcanonical RRKM rates were calculated to predict the time constant for the conversion from the anti conformer to the gauche conformer, and that for the reverse isomerization, to be  $\sim 13$  ps and  $\sim 3$  ps, respectively. These time constants yield a steady-state anti:gauche conformer ratio of  $\sim 83:17$ . On the other hand, assuming complete thermalization of the internal degrees of freedom gives a similar conformer ratio of 81:19, estimated from the energy difference between the conformers (calculated to be  $\sim 3.3$  kcal/mol<sup>32</sup>), and the internal temperature. In our refinements of the UED data, the anti:gauche conformer ratio of the  $C_2F_4I$  radicals was therefore held fixed at 81:19, close enough to the initial 76:24 ratio for the parent composition. Note that the quantum chemical calculations predicted that the conformational energy difference between anti and gauche radicals is *larger* than the corresponding value for the parent conformers ( $\sim 1.2$ – $1.9$  kcal/mol; see ref 32 and references therein). This larger energy difference apparently results from a relative stabilization of the anti radicals that has been rationalized in terms of hyperconjugation between the radical center and the  $\sigma^*(C-I)$  molecular orbital.<sup>33</sup>

Finally, the structural parameters for the  $C_2F_4$  product species were obtained from ref 34. The fraction refinements were thus simplified to a two-parameter fit: (1) the total fraction of  $C_2F_4I_2$  parent molecules depleted and (2) the total fraction of  $C_2F_4I$  radicals formed. The fraction of  $C_2F_4$  product formed could then be determined from these values at each time point according to eq 12

$$\Delta sM(t; -95 \text{ ps}; s) = -|\Delta p_{C_2F_4I_2}| \cdot sM(s)_{C_2F_4I_2} + |\Delta p_{C_2F_4I}| \cdot sM(s)_{C_2F_4I} + |\Delta p_{C_2F_4}| \cdot sM(s)_{C_2F_4} \quad (17)$$

with

$$\Delta p_{C_2F_4} + \Delta p_{C_2F_4I} = -\Delta p_{C_2F_4I_2} \quad (18)$$

The time evolution of the distribution of structures as determined from the  $\Delta sM(t; -95 \text{ ps}; s)$  data is shown in Figure 8. Figure 8(a) shows the time dependence of the relative fraction of the  $C_2F_4I_2$  parent molecules. An initial depletion of the parental signal is observed to follow the response function of the UED apparatus, a result that is consistent with the  $\sim 200$  fs time constant measured previously by femtosecond mass spectrometry.<sup>11</sup> The amplitude of the diffraction-difference signals, when scaled to that of the ground state, shows that  $\sim 8\%$  of the parent molecules participated in the reaction under the given experimental conditions. The temporal evolution of the relative fractions of the  $C_2F_4I$  radicals and  $C_2F_4$  products are shown respectively in Figure 8(b) and 8(c). The relative fraction of  $C_2F_4I$  rises briefly (within the response time of the apparatus) and then decays, whereas the fraction of  $C_2F_4$  rises steadily. Fitting these time-dependent fractions results in an average time constant of  $26 \pm 7$  ps for the depletion of  $C_2F_4I$  transient structures ( $20 \pm 5$  ps) and formation of  $C_2F_4$  molecules ( $31 \pm 4$  ps); the overall temporal resolution of the apparatus was explicitly included in the determination of these time constants. Given the available internal energy of the  $C_2F_4I$  intermediate described above, this temporal behavior is entirely consistent with a barrier crossing process, as is the percentage of  $C_2F_4I$  radicals undergoing further dissociation to form  $C_2F_4$  ( $55 \pm 5\%$ ).

**C. Structural Change, Intermediate to Product: The  $C_2F_4I \rightarrow C_2F_4 + I$  Process.** As shown in the previous section, any reaction involving the parent molecules is complete within the first 5 ps. Thus, to highlight the structural changes of the reaction intermediate and product only—with no contribution from any other species present—we generated a set of additional diffraction-difference curves with  $t_{\text{ref}} = 5$  ps through eq 12. Figure 9(a) shows raw difference curves [ $\Delta R^E(t; 5 \text{ ps}; s)$ ] and the corresponding residual background curves [ $\Delta R_B^E(t; 5 \text{ ps}; s)$ ]. The  $\Delta sM^E(t; 5 \text{ ps}; s)$  curves, created in part by subtracting the baseline curves obtained for each time point, are shown in Figure 9(b). As before, this difference procedure removes most of the background signal.

Figure 9(c) shows the corresponding difference radial distribution curves,  $\Delta f^E(t; 5 \text{ ps}; r)$ . The  $\Delta f(t; 5 \text{ ps}; r)$  signals arise only from the transient  $C_2F_4I$  and final product  $C_2F_4$  species, with the depletion of the  $C_2F_4I$  radical being evident at C–I, C $\cdots$ I, and F $\cdots$ I separations; note that the populations of other internuclear separations (e.g., C–F, C–C, and F $\cdots$ F) are essentially unchanged, and make no contribution to the  $\Delta sM^E(t; 5 \text{ ps}; s)$  or  $\Delta f^E(t; -95 \text{ ps}; r)$  signals. The absence of an I $\cdots$ I component ( $\sim 5.1$  Å) in the  $\Delta f^E(t; 5 \text{ ps}; r)$  curves clearly shows that we are observing solely the population change of the transient  $C_2F_4I$  structures forming  $C_2F_4$ , and that the contribution from the unreacted  $C_2F_4I_2$  population is negligible. Theoretical  $\Delta sM^T(t; 5 \text{ ps}; s)$  and  $\Delta f^T(t; 5 \text{ ps}; s)$  curves (red curves in Figure 9(b) and 9(c)) were obtained by a single-parameter fit (the fraction of  $C_2F_4$  species) of the experimental  $\Delta sM^E(t; 5 \text{ ps}; s)$  curves according to eq 12

$$\Delta sM(t; 5 \text{ ps}; s) = -|\Delta p_{C_2F_4I}| \cdot sM(s)_{C_2F_4I} + |\Delta p_{C_2F_4}| \cdot sM(s)_{C_2F_4} \quad (19)$$

with

$$\Delta p_{C_2F_4} = -\Delta p_{C_2F_4I} \quad (20)$$



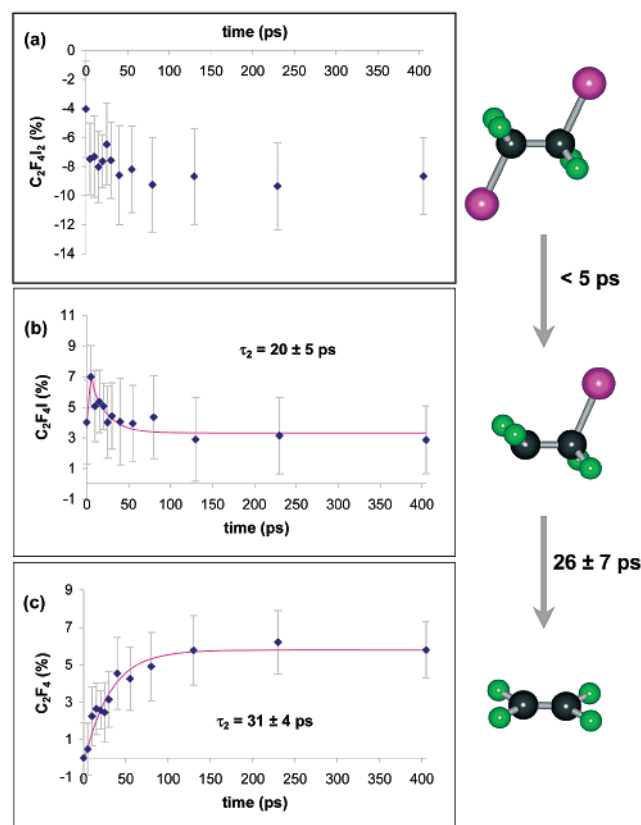


**Figure 8.** Time dependence of the species fractions from the analysis of  $\Delta sM(t; -95 \text{ ps}; s)$  data. (a) The depletion of the parent fraction (*anti* and *gauche*  $\text{C}_2\text{F}_4\text{I}_2$ ). Depletion of the parent signal is essentially complete within the  $\sim 5 \text{ ps}$  resolution of the experiment. (b) Time dependence of the transient  $\text{C}_2\text{F}_4\text{I}$  species. (c) Formation of the  $\text{C}_2\text{F}_4$  product. The time constants measured for the depletion of the  $\text{C}_2\text{F}_4\text{I}$  radicals ( $20 \pm 5 \text{ ps}$ ) and formation of  $\text{C}_2\text{F}_4$  molecules ( $31 \pm 4 \text{ ps}$ ) yields an average time constant of  $26 \pm 7 \text{ ps}$ . In all three figures, the temporal pulse widths of the electron and laser pulses were accounted for in the determination of the reported time constants. Each error bar (gray) represents one standard deviation. See Figure 10 for the improved sensitivity to the formation of  $\text{C}_2\text{F}_4$  structures and hence the improved signal-to-noise ratio.

The time-dependent fraction of  $\text{C}_2\text{F}_4$  formed after 5 ps, shown in Figure 10, yields a time constant of  $25 \pm 7 \text{ ps}$ , in total agreement with the above analysis of the  $\Delta f(t; -95 \text{ ps}; r)$  curves.

**D. Structure of the  $\text{C}_2\text{F}_4\text{I}$  Radical Intermediate.** The molecular structure of the  $\text{C}_2\text{F}_4\text{I}$  radical intermediate was determined from the diffraction-difference curves  $\Delta sM(t; 5 \text{ ps}; s)$ ; both bridged and classical  $\text{C}_2\text{F}_4\text{I}$  structures were considered in the fitting of the diffraction data. The symmetrically bridged structure has  $C_{2v}$  symmetry, whereas the *anti* and *gauche* conformers of the classical structure have  $C_s$  and  $C_1$  symmetry, respectively. The  $\Delta R^E(t; 5 \text{ ps}; s)$  difference curves from  $t = +40 \text{ ps}$  to  $+405 \text{ ps}$  were averaged (prior to Fourier filtering—see Figure 6(b)) to improve the precision of the fits, yielding the time-averaged curve,  $\Delta R^E(\infty; 5 \text{ ps}; s)$ . No significant changes in the structure of the radical are expected (or were observed) over this temporal range, as the internal energy of the radical should already be nearly equilibrated, and collisional cooling should not become important until well into the nanosecond regime under the present experimental conditions.

Prior to performing the time-averaged structural refinement for the  $\text{C}_2\text{F}_4\text{I}$  radical, preliminary structural refinements were performed at each point in time in order to detect the presence of time-dependent structural changes within the  $\text{C}_2\text{F}_4\text{I}$  species—manifested as far-from-equilibrium geometries<sup>8</sup> in the early

stages of the reaction. Most of the structural parameters showed little sign of temporal dependence, but the results for a few of the parameters were less conclusive. The C—I bond distance and  $\angle \text{CCI}$  bond angle showed the greatest evidence for time-dependent changes at early time points (not shown), but further investigation is necessary before a definitive conclusion can be made; future UED studies with improved sensitivity, resolution, and analysis should be better able to determine the significance of far-from-equilibrium geometries in this reaction.

The  $\Delta R^E(\infty; 5 \text{ ps}; s)$  signal was fit separately with starting structural parameters predicted from calculations for either the bridged species, or the 81:19 mixture of the classical (*anti* and *gauche*) species. The  $\Delta R^E(\infty; 5 \text{ ps}; s)$  curve, along with the background curve obtained by fitting through the theoretical zero-crossing points, is shown in Figure 6(c). The results of this fitting procedure are contained in Figure 11, where the experimental  $\Delta sM^E(\infty; 5 \text{ ps}; s)$  and  $\Delta f^E(\infty; 5 \text{ ps}; r)$  curves are shown along with the corresponding theoretical curves produced with the quantum chemical structures. As shown in Figure 11(c) and 11(d), the theoretical curves for the mixture of classical structures reproduce the experimental data extremely well, whereas the fit provided by the theoretical bridged structure (Figure 11(a) and 11(b)) is vastly inferior. Indeed, the  $\Delta sM^E(\infty; 5 \text{ ps}; s)$  and  $\Delta sM^T(\infty; 5 \text{ ps}; s)$  curves in Figure 11(a) clearly go out of phase, yielding manifestly different positions for the two prominent negative peaks in the corresponding  $\Delta f^E(\infty; 5 \text{ ps}; r)$  and  $\Delta f^T(\infty; 5 \text{ ps}; r)$  curves (Figure 11(b)). Thus, we conclude that the structure of the  $\text{C}_2\text{F}_4\text{I}$  radical intermediate is in fact classical in nature,<sup>4</sup> in general agreement with previous qualitative analysis from second-generation (UED2) experiments.<sup>3</sup>

Significant improvements in sensitivity and resolution provided by the UED3 apparatus permitted quantitative determination of the molecular structure of the  $\text{C}_2\text{F}_4\text{I}$  radical from our experimental data, thereby allowing a direct comparison with quantum chemical calculations. A least-squares refinement of the  $\Delta sM^E(\infty; 5 \text{ ps}; s)$  data was performed as follows. Reasonable assumptions were made to simplify the fit and reduce the number of adjustable parameters in the final structural refinement, as described below. Assuming a torsion angle of  $180^\circ$ , the *anti* conformer of the  $\text{C}_2\text{F}_4\text{I}$  radical has 9 independent parameters—four covalent bond distances and five bond angles—when the structure is constrained to be geometrically consistent. The remaining (dependent) internuclear separations were obtained via trigonometric relations constructed in terms of the chosen independent parameters. The *gauche* conformer was treated similarly: it was described by the same 9 independent parameters, but with values differing from those of the *anti* conformers by small constant amounts, as predicted by quantum chemical calculations.<sup>32</sup> For example, the calculations suggested that the C—I distance of the *gauche* conformer [ $r(\text{C—I})_{\text{gauche}}$ ] would be less than that of the *anti* conformer by  $0.015 \text{ \AA}$ ; thus,  $r(\text{C—I})_{\text{gauche}}$  was obtained by subtracting  $0.015 \text{ \AA}$  from the refined value of  $r(\text{C—I})_{\text{anti}}$ . Again, following theoretical predictions, the primary dihedral angle of the *gauche* species was fixed at  $56^\circ$  as the dihedral angle was relatively insensitive in the fitting, partially due to the low amount of *gauche* structures present.

As before, the *anti*:*gauche* radical conformer ratio was held fixed at 81:19 (see section IV B). The values for the mean amplitudes of vibration ( $l$ ) and centrifugal distortion corrections ( $dr$ ) for each atom—atom pair (summarized in Table 1) were calculated using the ASYM40 program developed by Hedberg and co-workers<sup>29</sup> (assuming a thermal distribution of the internal energy within the  $\text{C}_2\text{F}_4\text{I}$  radical). These values were then entered

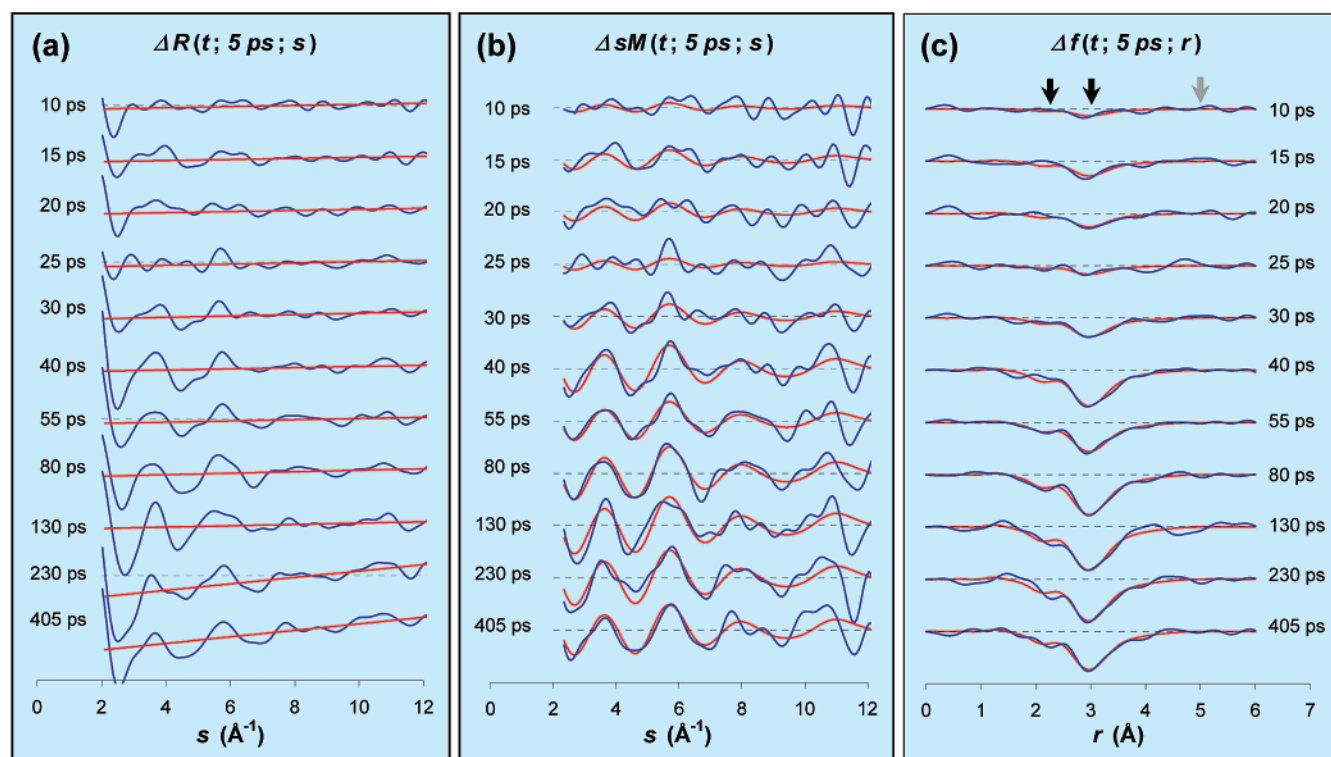


**Figure 9.** Time-resolved structural changes involving only the  $\text{C}_2\text{F}_4\text{I} \rightarrow \text{C}_2\text{F}_4 + \text{I}$  contribution to the diffraction-difference signal. (a) Raw diffraction-difference signals,  $\Delta R(t; 5 \text{ ps}; s)$ , (blue curves), shown with the (nearly linear) baseline curves (red). (b) Experimental (blue) and theoretical (red)  $\Delta sM(t; 5 \text{ ps}; s)$  curves obtained at varying time delays. (c) Corresponding experimental (blue) and theoretical (red)  $\Delta f(t; 5 \text{ ps}; r)$  curves. Note the absence of a peak at  $\sim 5.1 \text{ \AA}$  corresponding to the depletion of  $\text{I}\cdots\text{I}$  internuclear distances (gray arrow).

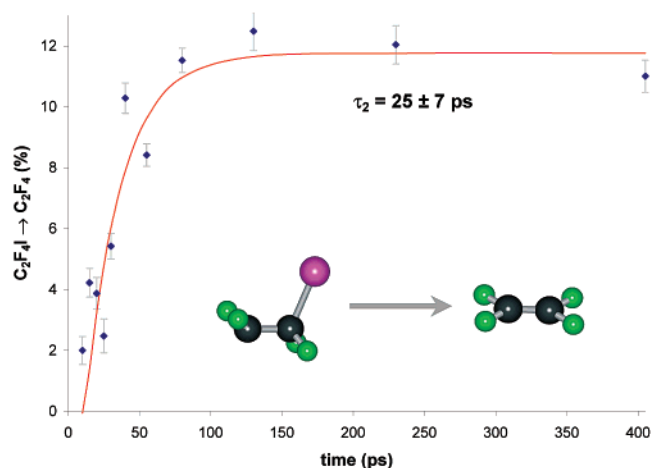


**Figure 10.** Time dependence of the formation of  $\text{C}_2\text{F}_4$  molecules from the decay of  $\text{C}_2\text{F}_4\text{I}$  transient structures in the  $\Delta sM(t; 5 \text{ ps}; s)$  data. The curve is an exponential fit of the  $\text{C}_2\text{F}_4$  fraction (with the temporal pulse widths of the electron and laser pulses taken into account); the apparent time constant for the formation of  $\text{C}_2\text{F}_4$  was of  $25 \pm 7 \text{ ps}$ . Each error bar represents one standard deviation. Note that the apparent signal does not grow from zero since the data represent a change only after  $5 \text{ ps}$ .

into the structural refinement of the (geometrically consistent) internuclear distances (at the potential minima,  $r_e$ ) and the bond angles using the relation  $r_a \approx r_e + (3/2)al^2 + dr - l^2/r$ , where  $r_a$  is the internuclear distance as measured by electron diffraction [ $r_{ij}$  in eq 4] and  $a$  is the anharmonicity constant for the bond. The independent structural parameters obtained from the least-squares fit of the experimental data could then be compared to quantum chemical calculations.

The results of the least-squares structural refinement are shown in Figure 12, and the values determined for the inde-

pendent structural parameters are summarized in Table 2. The corresponding error matrix is given in Table 3; the diagonal elements of the matrix are the squares of the standard deviations of the least-squares refinement, and the off-diagonal elements are the average products of standard deviations for each pairing of refined parameters. The  $r_e(\text{C}-\text{I})$  and  $r_e(\text{C}-\text{C})$  distances of the  $\text{C}_2\text{F}_4\text{I}$  radical are, respectively, longer and shorter than those of the parent molecule (for  $\text{C}_2\text{F}_4\text{I}_2$ ,  $r_e(\text{C}-\text{I}) \approx 2.136 \text{ \AA}$ ,  $r_e(\text{C}-\text{C}) \approx 1.534 \text{ \AA}$ ),<sup>31</sup> whereas the  $\text{C}-\text{F}'$  internuclear distance in the radical site ( $-\text{CF}'_2$ ) is shorter than that of the  $-\text{CF}_2\text{I}$  site. Moreover, the  $\angle\text{CCF}'$  and  $\angle\text{F}'\text{CF}'$  angles become larger than the corresponding angles of the parent (by  $\sim 9^\circ$  and  $\sim 12^\circ$ , respectively<sup>31</sup>), suggesting that the radical center ( $-\text{CF}'_2$ ) of the  $\text{C}_2\text{F}_4\text{I}$  intermediate relaxes following loss of the first I atom (naturally, a similar comparison may be drawn between these  $\angle\text{CCF}'$  and  $\angle\text{F}'\text{CF}'$  angles and the  $\angle\text{CCF}$  and  $\angle\text{FCF}$  angles on the other side of the radical). These results are consistent with the increased  $\text{C}-\text{C}$  bond order expected from the formation of the transient  $\text{C}_2\text{F}_4\text{I}$  structure. These trends were also well-reproduced by the quantum chemical calculations; indeed, the refined internuclear distances reported in Table 2 agree with the corresponding theoretical predictions to within  $0.03 \text{ \AA}$ .<sup>32</sup>

It is interesting to compare the molecular structure of the  $\text{C}_2\text{F}_4\text{I}$  radical with that of the  $\text{C}_2\text{H}_4\text{I}$  radical, and consider the stereochemical implications for these intermediate species. However, although the geometry of the  $\text{C}_2\text{F}_4\text{I}$  radical has now been studied with UED (see also refs 3,4), to date only quantum chemical investigations of the  $\text{C}_2\text{H}_4\text{I}$  radical geometry have been performed (the high thermal instability of the  $\text{C}_2\text{H}_4\text{I}_2$  parent molecule makes this substance notoriously difficult to work with in experimental studies). Quantum chemical structures of the  $\text{C}_2\text{F}_4\text{I}$  radical and the  $\text{C}_2\text{H}_4\text{I}$  radical are presented in Figure 13, along with the corresponding energy contour maps calculated for both structures.<sup>16,32</sup> The energy contour maps, calculated

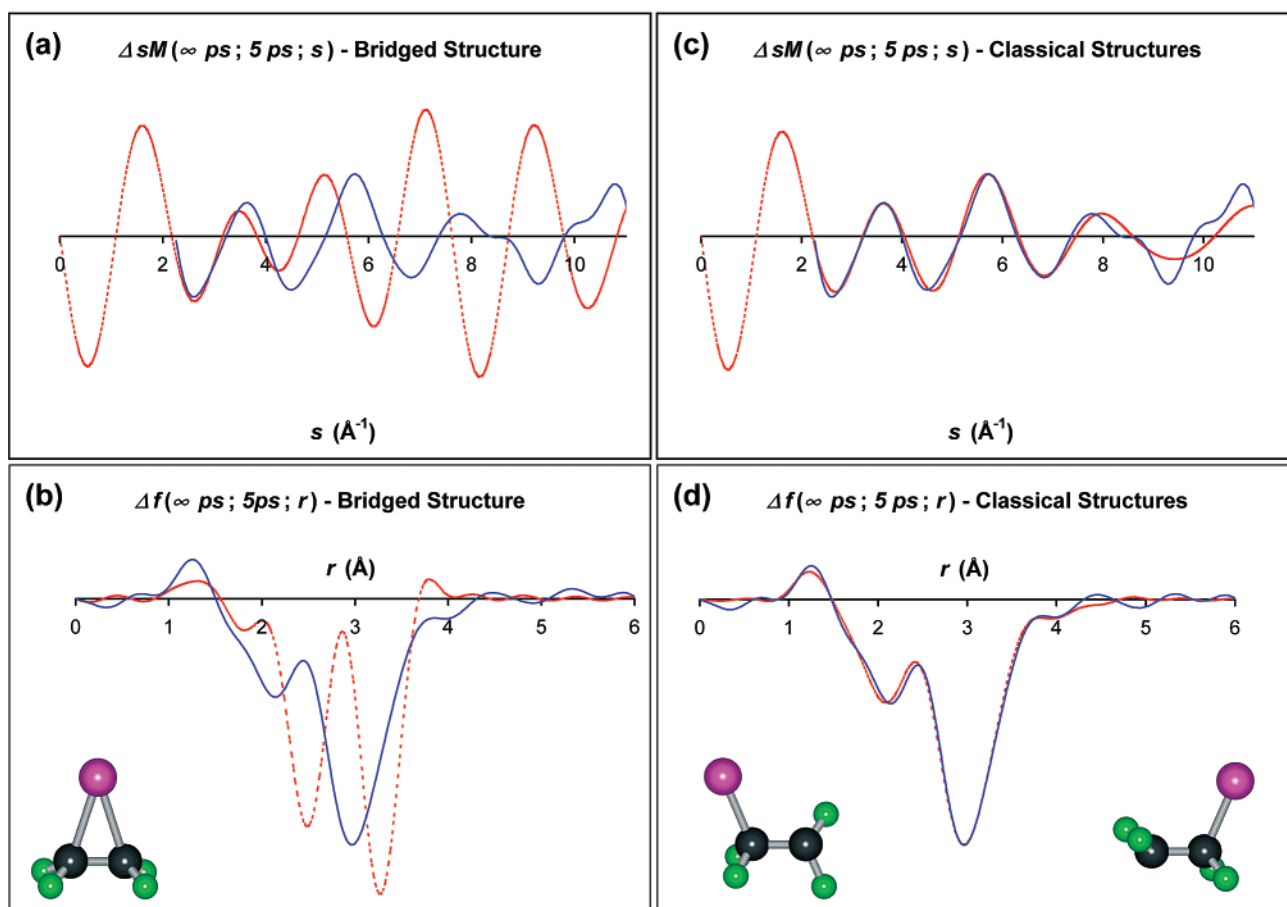


**Figure 11.** Structure of the  $\text{C}_2\text{F}_4\text{I}$  radical intermediate.<sup>4</sup> (a,b) Comparison of experimental  $\Delta sM(\infty \text{ ps}; 5 \text{ ps}; s)$  and  $\Delta f(\infty \text{ ps}; 5 \text{ ps}; r)$  curves (blue) with corresponding theoretical curves (red) generated with starting structural parameters of bridged  $\text{C}_2\text{F}_4\text{I}$  obtained via calculations. (c,d) Comparison of experimental  $\Delta sM(\infty \text{ ps}; 5 \text{ ps}; s)$  and  $\Delta f(\infty \text{ ps}; 5 \text{ ps}; r)$  curves with theoretical curves obtained using the predicted classical (anti and gauche)  $\text{C}_2\text{F}_4\text{I}$  structures.

**TABLE 1: Mean Amplitudes of Vibration ( $l$ ) and Centrifugal Distortions ( $dr$ ) at 800 K for the Anti Conformer of the  $\text{C}_2\text{F}_4\text{I}$  Radical as Calculated Using the ASYM40 Program<sup>29a</sup>**

	$l$ (Å)	$dr$ (Å)
$\text{C}_1-\text{C}_2$	0.0657	0.0010
$\text{C}_1-\text{I}_5$	0.0889	0.0025
$\text{C}_2-\text{I}_5$	0.1268	0.0060
$\text{C}_1-\text{F}_3$	0.0572	0.0004
$\text{C}_2-\text{F}_6$	0.0590	0.0006
$\text{C}_2-\text{F}_3$	0.0983	0.0006
$\text{C}_1-\text{F}_6$	0.1148	0.0030
$\text{F}_3-\text{F}_4$	0.0886	0.0002
$\text{F}_6-\text{F}_7$	0.0844	0.0001
$\text{F}_3-\text{F}_6$	0.2047	0.0025
$\text{F}_3-\text{F}_7$	0.0999	0.0020
$\text{F}_3-\text{I}_5$	0.1193	0.0018
$\text{F}_6-\text{I}_5$	0.3307	0.0101

<sup>a</sup> The atomic numbering follows the schematic.

using density functional theory (DFT) methods (B3PW91,<sup>35,36</sup> with the LAV3P basis set), were generated by optimizing the molecular geometry as a function of the position of the primary halogen atom (I); in both calculations, the position of the I atom was constrained to lie in the ICC plane bisecting the  $\angle\text{RCR}$

angles (with  $\text{R}=\text{H}$  or  $\text{F}$ ). The dramatic difference between the  $\text{C}_2\text{F}_4\text{I}$  and  $\text{C}_2\text{H}_4\text{I}$  radical geometries in these calculations originated from the lower  $\pi$  electron density of the  $\text{C}_2\text{F}_4$  moiety compared to that of the  $\text{C}_2\text{H}_4$  moiety (due to electron withdrawal by the electronegative F atoms), which in turn affects the interaction between the p orbital of the primary halogen atom (I) and the  $\pi$  orbital of the C–C bond in the bridged structure.

Recent theoretical investigations<sup>16,32</sup> generalized this structural comparison to include a variety of  $\text{CR}_2\text{XCR}_2$ -type radicals, where R represents either H or F, and X refers to the heavy halides (Cl, Br, and I). These calculations predicted that when  $\text{R}=\text{F}$ , then the most energetically stable radical structure is classical (with anti conformers always more stable than gauche conformers); indeed, no minimum-energy structures with bridged geometries could be found for these species without at least one imaginary frequency (with the exception of  $\text{CF}_2\text{ClCF}_2$  at the Hartree–Fock level). However, varying results were obtained with  $\text{R}=\text{H}$ : when  $\text{X}=\text{I}$ , then the most stable structure is predicted to be bridged (Figure 13); when  $\text{X}=\text{Cl}$ , the most stable structure is classical; and when  $\text{X}=\text{Br}$ , the result depends on the computational method used—B3PW91 DFT calculations using the LAV3P basis set predicted that the most stable structure would be bridged, but the same calculation using the LAV3P(d) basis set (which has an additional d orbital for the X atom) predicted a classical geometry for the global minimum (consistent with the results of a MRD-CI calculation performed elsewhere<sup>37</sup>).

Much of the interest in the molecular structures of  $\text{CR}_2\text{XCR}_2$ -type radicals lies in the relevance of structure and dynamics to



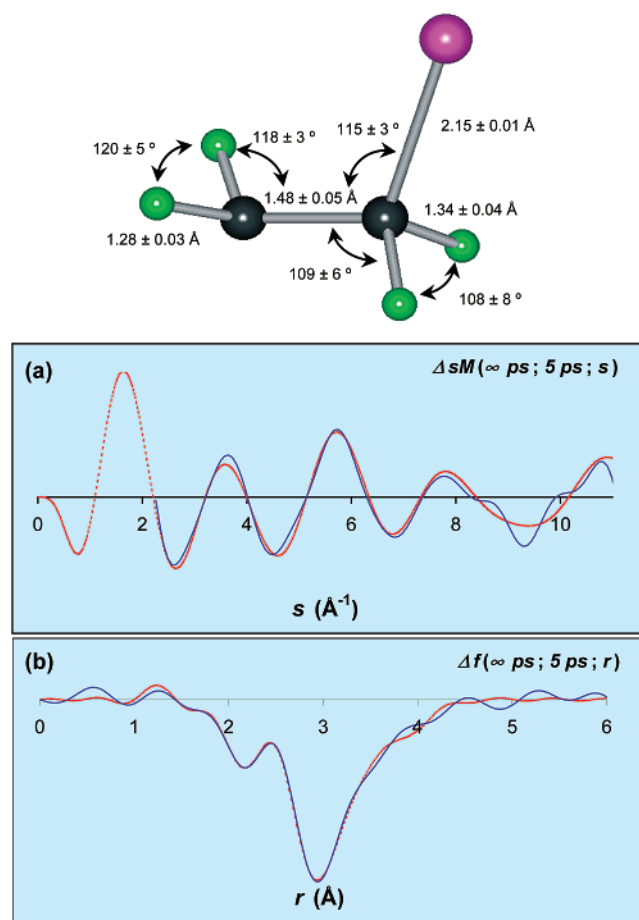


**Figure 12.** Refinement of the  $C_2F_4I$  radical structure. (a,b) Comparison of experimental  $\Delta sM(\infty; 5 \text{ ps}; s)$  (a) and  $\Delta f(\infty; 5 \text{ ps}; r)$  (b) curves (blue) with corresponding theoretical curves (red) obtained from the least-squares refinement of the  $C_2F_4I$  structure (see text). Values for some of the major structural parameters (of the anti conformer) are indicated in the ball-and-stick model of the radical.

**TABLE 2: Comparison of the Experimental Values of the Independent Structural Parameters of the Classical  $C_2F_4I$  Radical Intermediate with Those Obtained via Quantum Chemical Calculations<sup>32a</sup>**

	experiment	predicted values	
	<i>anti</i>	<i>anti</i>	<i>gauche</i>
$r(C=C)$	$1.478 \pm 0.049$	1.503	1.508
$r(C-F)$	$1.340 \pm 0.037$	1.322	1.327, 1.323
$r(C-I)$	$2.153 \pm 0.013$	2.164	2.149
$r(C-F')$	$1.277 \pm 0.027$	1.304	1.309, 1.307
$\angle CCI$	$115.0 \pm 3.1$	112.7	111.8
$\angle CCF$	$108.6 \pm 6.0$	108.6	109.8, 108.1
$\angle FCF/2$	$54.0 \pm 5.6$	54.4	54.0
$\angle CCF'$	$117.9 \pm 3.1$	114.0	112.3, 113.8
$\angle F'CF'/2$	$59.9 \pm 3.9$	55.9	55.6

<sup>a</sup> The bond distances are in ångströms and the bond angles are in degrees.

the stereochemistry of reactions involving these transient species. For example, consider the generalized two-step elimination of  $2X$  from  $C_2R_4X_2$  giving  $C_2R_4$ , shown schematically in Figure 14. A number of  $C_2R_4X$  intermediate structures could, in principle, be involved in the reaction, with different implications for the stereochemical control of the reaction with regard to the final positions of the  $-R$  groups about the  $C=C$  bond in the  $C_2R_4$  product. The formation of a bridged  $C_2R_4X$  structure prevents rotation about the  $C-C$  bond, thereby ensuring stereochemical control in accordance with the Skell hypoth-

esis<sup>17,18</sup> (a similar result would be obtained if the  $X$  atom were rapidly "shuttled" between the two  $-CR_2$  moieties<sup>19</sup>). Alternatively, a classical structure could be formed, with either a "pyramidal" radical center (predicted for  $R=F$ <sup>32</sup>) or a nearly planar radical center (predicted for  $R=H$ <sup>32</sup>). Because rotation about the  $C-C$  bond is unhindered in classical structures, one might predict (contrapositively to the Skell hypothesis) that reactions involving  $C_2R_4X$  radical intermediates that lack bridged geometries would *not* maintain stereochemical control (for nearly planar radical centers ( $R=H$ ), the final positions of  $-R_3$  and  $-R_4$  could be scrambled through simple rotation about the  $C-C$  bond, whereas in species with  $R=F$  the nonplanar nature of the  $-CF_2$  moiety might require some combination of rotation and inversion due to the high energy required to reach the "eclipsed" rotational transition state<sup>32</sup>).

However, it should be considered that dynamical effects may also play a role in the retention of stereochemistry in such reactions; if the time for the second  $C-X$  bond breakage is shorter than that of rotation around the  $C-C$  bond, stereochemistry will be retained even in reactions involving classical  $C_2R_4X$  structures. Future studies on other  $C_2R_4X$  species may shine new light on the respective roles of structure and dynamics in determining the stereochemical nature of the products formed by various reactions.

## V. Concluding Remarks

In summary, significant improvements in instrumentation provided by our third generation apparatus now permit UED to study structural dynamics in chemical reactions with unprecedented temporal and spatial resolution. These experimental advances have been accompanied by improvements in data processing and use of the diffraction-difference analysis, which were described here in detail. These advances were borne out in the first application of the new apparatus—the study of the nonconcerted elimination of iodine from  $C_2F_4I_2$ . The structural changes occurring over the course of the reaction were followed with temporal resolution of  $\sim 5$  ps, with spatial resolution approaching  $0.01$  Å, and with a sensitivity to chemical change of  $\sim 1\%$ . The high sensitivity and spatiotemporal resolution permitted the molecular structure of the transient intermediate  $C_2F_4I$  to be determined and refined: the radical is classical, not bridged, in nature—in quantitative agreement with quantum chemical predictions to within  $0.03$  Å. In the future, additional UED studies of other  $C_2R_4X$  intermediates and related species should provide considerable insight into the respective roles of structure and dynamics in stereochemical control. Finally, with the recent UED observations in this laboratory of structural evolution in cyclic organic molecules,<sup>4,8</sup> organometallics,<sup>6</sup> and aromatics,<sup>9</sup> it has been demonstrated that UED is a general probe of transient molecular structures in complex reactions, including those *without* the involvement of highly scattering heavy atoms. The technique thus promises to open a new window into the fundamental structural dynamics underlying various types of physical and chemical processes.

**Acknowledgment.** This work was supported by the National Science Foundation and the Air Force Office of Scientific Research. We gratefully acknowledge U. Gomez for his work in the primary construction of the UED3 apparatus. We also thank C.-Y. Ruan and D. Zhong for helpful discussions.

## Appendix

**A. CCD Image Processing.** The digital nature of our data acquisition permits the use of a variety of powerful image

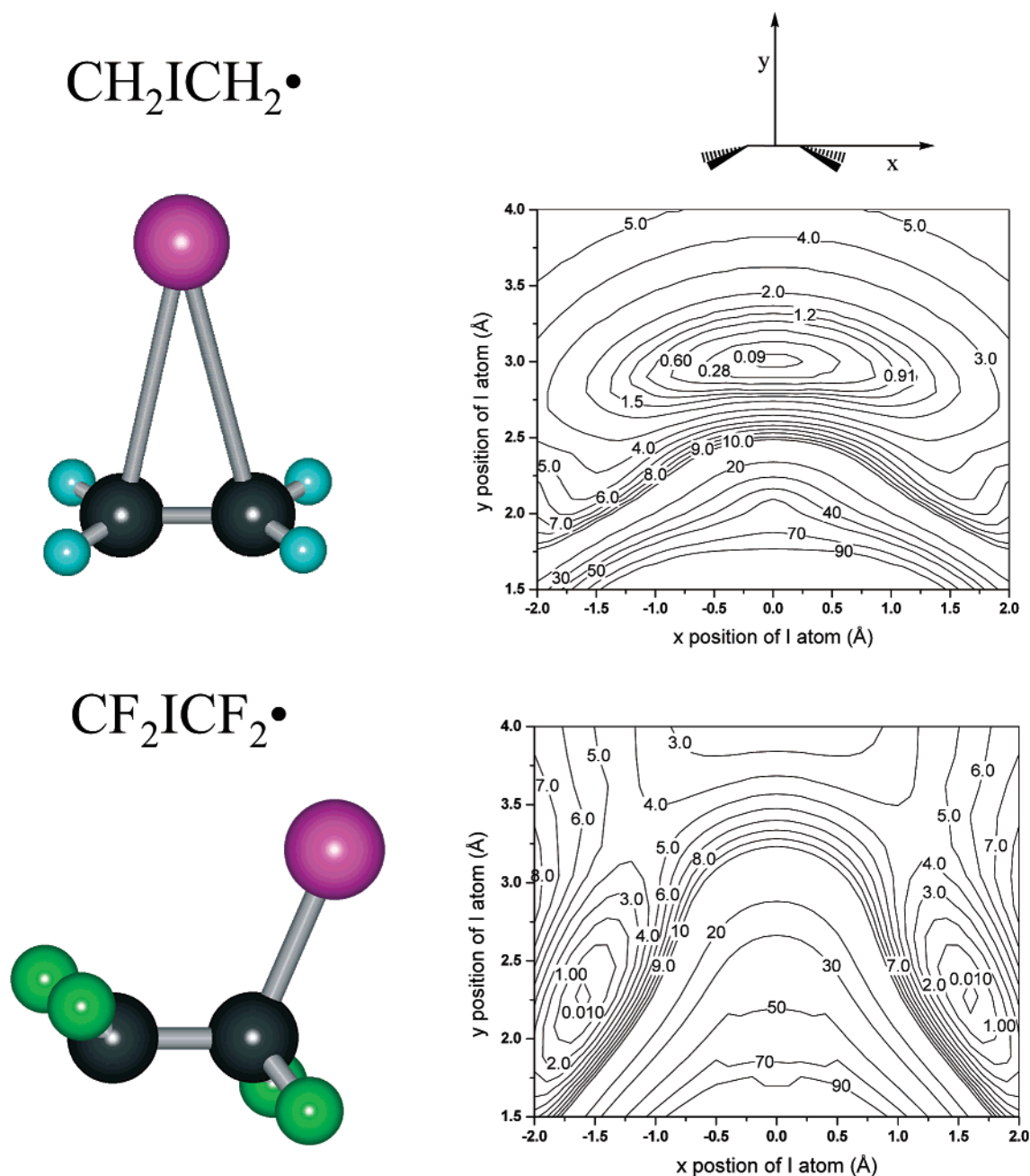


**Figure 13.** Comparison of the theoretical molecular structures of the  $\text{C}_2\text{H}_4\text{I}$  and  $\text{C}_2\text{F}_4\text{I}$  radical intermediates, along with the corresponding energy contour maps obtained via density functional theory calculations [using the B3PW91(LAV3P) method].<sup>16,32</sup> Each map, which indicates the relative energy corresponding to the position of the iodine atom with respect to the two carbon atoms, manifests the nature of the given species:  $\text{C}_2\text{F}_4\text{I}$  is predicted to be classical, whereas  $\text{C}_2\text{H}_4\text{I}$  is predicted to be bridged.

**TABLE 3: Error Matrix for the Least-Squares Refinement of the  $\text{C}_2\text{F}_4\text{I}$  Radical Intermediate Structure**

	$r(\text{C}-\text{C})$	$r(\text{C}-\text{F})$	$r(\text{C}-\text{I})$	$r(\text{C}-\text{F}')$	$\angle\text{CCI}$	$\angle\text{CCF}$	$\angle\text{FCF}/2$	$\angle\text{CCF}'$	$\angle\text{F}'\text{CF}'/2$
$r(\text{C}-\text{C})$	0.0024	-0.0018	-0.0005	0.0012	-0.1488	-0.2898	0.2669	0.1420	-0.1814
$r(\text{C}-\text{F})$		0.0014	0.0003	-0.0010	0.1121	0.2160	-0.1990	-0.1058	0.1352
$r(\text{C}-\text{I})$			0.0002	-0.0002	0.0284	0.0587	-0.0515	-0.0234	0.0309
$r(\text{C}-\text{F}')$				0.0007	-0.0797	-0.1540	0.1413	0.0742	-0.0956
$\angle\text{CCI}$					9.6844	18.4113	-17.1247	-9.3730	11.7735
$\angle\text{CCF}$						35.8866	-33.1673	-17.8859	22.6619
$\angle\text{FCF}/2$							30.8816	16.8453	-21.3019
$\angle\text{CCF}'$								9.8962	-12.0551
$\angle\text{F}'\text{CF}'/2$									15.1277

processing techniques that aid in the isolation of molecular diffraction signals. At each given time delay between pump (laser) and probe (electron) pulses, a series of 2-D diffraction images ( $A_i$ ,  $i = 1, 2, \dots, n$ ) are acquired with the CCD camera (here, bold characters denote 2-D images). The first step in the

image processing is to generate an averaged 2-D image, from which unwanted random events have been removed; such events may be caused, for example, by spontaneous emission and cosmic rays. The averaged image,  $A'$ , is created according to the iterative procedure described below.

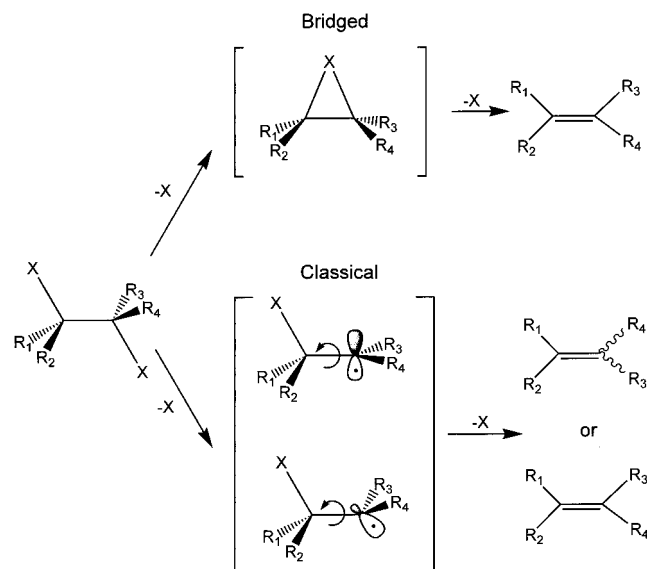


**Figure 14.** Schematic of dihalide elimination reactions involving  $C_2R_4X$  radical intermediates. Once the parent molecule  $C_2R_4X_2$  loses the first  $-X$  atom, the intermediate species  $C_2R_4X$  is formed. In the case of a bridged intermediate structure (top brackets), the retention of stereochemical selectivity is derived from the inhibition of rotation about the  $C-C$  bond (top product). However, in the case of the classical structure (bottom brackets), the situation is more complex. Rotation about the  $C-C$  bond is allowed; if the time scale for the elimination of the second  $-X$  atom is much faster than the rotation, one can expect stereochemical selectivity (bottom product), whereas stereochemical control would be lost if the situation were reversed (middle product). With regard to the geometry of the radical site in the classical structure, simple rotation about the  $C-C$  bond (prior to the loss of the second  $-X$  atom) would suffice for the loss of stereochemical control for structures with planar radical centers (middle intermediate), whereas species with nonplanar radical centers (bottom intermediate) may require a combination of rotation and inversion.

A key trait of our 2-D data is the accessibility of the individual pixels in the digitized images, which allows us to treat each pixel as an independent detector statistically characterized by its own mean intensity and standard deviation. For each  $A_i$ , a corresponding binary “mask” image,  $M_i$ , is created. For example, a given pixel with coordinates  $(x,y)$  in each  $M_i$  has a value of *one* if the corresponding pixel in the diffraction image  $A_i$  is valid (the conditions for validity are outlined below), or has a value of *zero* otherwise. We define  $M_i(x,y)$  as that pixel in a given  $M_i$  with coordinates  $(x,y)$ ; initially,  $M_i(x,y) = 1$  for all pixels in all  $n$  mask images.

In the first step of each processing loop, an average value for the signal intensity at each pixel,  $\bar{A}(x,y)$ , is obtained over the  $n$  raw diffraction images

$$\bar{A}(x,y) = \frac{\sum_i^n M_i(x,y) \cdot A_i(x,y)}{\sum_i^n M_i(x,y)} \quad (A1)$$

where  $A_i(x,y)$  is the signal intensity for the pixel with coordinates  $(x,y)$  in the  $i$ th diffraction image ( $A_i$ ), and the sum  $\sum_i^n M_i(x,y)$  gives the number of valid pixels over all  $A_i$  with coordinates  $(x,y)$ . During this step  $\bar{A}(x,y)$  and  $\sigma(x,y)$  (the standard deviation of the averaged scattering intensity) are calculated for each pixel in the average image  $\bar{A}$ . To remove the signal spikes from random events, each diffraction image  $A_i$  is then submitted to

a pixel-by-pixel rejection criterion requiring that the value of given pixel  $A_i(x,y)$  lies within four standard deviations of the average value for that pixel (i.e., that  $\bar{A}(x,y) - 4\sigma(x,y) \leq A_i(x,y) \leq \bar{A}(x,y) + 4\sigma(x,y)$ ). If a given value for  $A_i(x,y)$  does not meet this criterion, then this pixel is declared invalid, and the value of  $M_i(x,y)$  in the corresponding mask image  $M_i$  is set to zero—thereby preventing this pixel from contributing to the averaged signal in the next processing loop. This cycle is typically repeated three times, with the  $\bar{A}(x,y)$  values,  $\sigma(x,y)$  values, and the  $M_i$  mask images updated after each cycle.

At the conclusion of the last cycle, the final 2-D binary mask ( $M'$ ) is generated. Pixels in  $M'$  corresponding to inactive regions of the CCD camera (and pixels manually removed due to systematic problems) are set to zero, thereby ensuring that these regions do not contribute to the final diffraction signal when the averaged  $\bar{A}$  image is multiplied by this final mask. This process yields the final, processed averaged image,  $\bar{A}'$ , which is now used for all further analysis. All averaged images, including background images and the reference gas images, were generated by this procedure.

Next, an averaged background image ( $\bar{B}'$ ), obtained under identical conditions as the molecular diffraction image (e.g., exposure time, laser light scattering, etc.)—except *without* the presence of the gas sample under study—is then subtracted from  $\bar{A}'$ . After this background subtraction, the 2-D diffraction image is then divided by a corresponding ref 2-D image,  $\bar{X}'$ , obtained from a monatomic gas (xenon)

$$R^{2D} = \frac{\bar{A}' - \bar{B}'}{\bar{X}' - \bar{B}_x'} \quad (A2)$$

where  $\bar{B}_x'$  is the corresponding background image for  $\bar{X}'$ . This division by the smoothly decaying diffraction intensity<sup>38</sup> of the atomic reference gas not only permits the direct visualization of molecular interferences (rings) in the 2-D “ratio” images,  $R^{2D}$  (see Figure 3), but also removes most of the systematic errors associated with the apparatus function of the detector. Each  $R^{2D}$  is then converted to an experimental 1-D total intensity curve,  $R^E(\text{pix})$ , by calculating the average intensity as a function of pixel radius,  $\rho(\text{pix})$ , from the electron beam center, according to the relation

$$\sqrt{x^2 + y^2} < \rho < \sqrt{(x+1)^2 + (y+1)^2} \quad (A3)$$

Corresponding values for the standard deviation of the scattering intensity at each pixel radius,  $\sigma(\text{pix})$ , are also calculated, permitting an additional round of spike rejection in the final calculation of  $R^E(\text{pix})$ . The  $\sigma(\text{pix})$  values are then used later as the weighting function in least-squares refinements (see section III D). Finally,  $R^E(\text{pix})$  is converted to  $R^E(s)$  by calculating the scattering angle  $\theta$  from the pixel dimensions and the camera length  $L$  (which is defined as the distance between the scattering volume beneath the sample nozzle and the detection screen). The camera length for these experiments was 13.39 cm, and was calibrated by comparing experimentally derived diffraction data obtained from high-purity nitrogen gas with literature values.<sup>23</sup> The division by the reference gas scattering intensity is accounted for by multiplying  $R^E(s)$  by the theoretical scattering intensity of the reference gas,  $I_{\text{ref}}^T(s)$

$$I^E(s) = R^E(s) \times I_{\text{ref}}^T(s) \quad (A4)$$

The experimental 1-D diffraction curves,  $I^E(s)$ , may then be analyzed according to the procedures described in section III



to generate the  $sM^E(s)$  and  $f(r)$  curves that reflect the structural features of the molecules under study.

**B. Normalization of Time-Dependent Diffraction Signals.** Before analyzing time-dependent diffraction signals, we normalize the total intensity of each time-dependent 2-D image,  $\bar{A}'(t)$ . This normalization procedure removes any systematic variation ( $\sim 1\%$  or less) in electron scattering intensity as a function of temporal delay (e.g., resulting from minuscule changes in photon flux at the photocathode as the delay line retroreflector is placed at different positions). The normalization is performed by first calculating the mean intensity of each image,  $\langle \bar{A}'(t) \rangle$ , according to the relation

$$\langle \bar{A}'(t) \rangle = \frac{\sum_{x,y}^{512} M'(x,y;t) \cdot \bar{A}'(x,y;t)}{\sum_{x,y}^{512} M'(x,y;t)} \quad (\text{A5})$$

where  $\bar{A}'(x,y;t)$  is the signal intensity at the pixel with coordinates  $(x,y)$  in the averaged 2-D image acquired at time delay  $t$ ,  $M'(t)$  is the binary mask image corresponding to the diffraction image  $\bar{A}'(t)$ , and 512 is the effective number of pixels along both  $x$  and  $y$  (our CCD camera has  $1024 \times 1024$  pixels, but  $2 \times 2$  binning is typically employed). The quantity  $\langle \bar{A}'(t) \rangle^{-1}$  obtained at each time delay is then used as the normalization constant for the corresponding averaged 2-D image. Once normalization has been performed, the diffraction difference method can be employed—see section III C for details.

## References and Notes

- (1) Williamson, J. C.; Zewail, A. H. *Proc. Natl. Acad. Sci.* **1991**, 88, 5021.
- (2) Williamson, J. C.; Cao, J.; Ihee, H.; Frey, H.; Zewail, A. H. *Nature* **1997**, 386, 159.
- (3) Cao, J.; Ihee, H.; Zewail, A. H. *Proc. Natl. Acad. Sci. U.S.A.* **1999**, 96, 338.
- (4) Ihee, H.; Lobastov, V. A.; Gomez, U.; Goodson, B. M.; Srinivasan, R.; Ruan, C.-Y.; Zewail, A. H. *Science* **2001**, 291, 458.
- (5) Helliwell, J. *Phys. World* **2001**, 14, 25.
- (6) Ihee, H.; Cao, J.; Zewail, A. H. *Angew. Chem., Int. Ed. Engl.* **2001**, 40, 1532.
- (7) Dudek, R. C.; Weber, P. M. *J. Phys. Chem. A* **2001**, 105, 4167.
- (8) Ruan, C.-Y.; Lobastov, V. A.; Srinivasan, R.; Goodson, B. M.; Ihee, H.; Zewail, A. H. *Proc. Natl. Acad. Sci. U.S.A.* **2001**, 98, 7117.
- (9) Lobastov, V. A.; Srinivasan, R.; Goodson, B. M.; Ruan, C.-Y.; Feenstra, J. S.; Zewail, A. H. *J. Phys. Chem. A*, **2001**, 105, 11 159.
- (10) Khundkar, L. R.; Zewail, A. H. *J. Chem. Phys.* **1990**, 92, 231.
- (11) Zhong, D.; Ahmad, S.; Zewail, A. H. *J. Am. Chem. Soc.* **1997**, 119, 5978.
- (12) *Free Radicals*; Kochi, J. K., Ed.; John Wiley & Sons: New York, 1973; Vol. II.
- (13) Beckwith, A. L. J.; Ingold, K. U. *Free-Radical Rearrangements. In Rearrangements in Ground and Excited States*; Mayo, P. d., Ed.; Academic Press: New York, 1980.
- (14) *Handbook of Bimolecular and Termolecular Gas Reactions*; Kerr, J. A., Ed.; CRC Press: Boca Raton, FL, 1981; Vol. I.
- (15) *Free Radicals in Organic Chemistry*; Fossey, J., Lefort, D., Sorba, J., Eds.; John Wiley & Sons: New York, 1995.
- (16) Ihee, H.; Zewail, A. H.; Goddard, W. A., III. *J. Phys. Chem. A* **1999**, 103, 6638.
- (17) Skell, P. S.; Tuleen, D. L.; Readio, P. D. *J. Am. Chem. Soc.* **1963**, 85, 2849.
- (18) Skell, P. S.; Shea, K. J. *Bridged Free Radicals. In Free Radicals*; Kochi, J. K., Ed.; John Wiley & Sons: New York, London, Sydney, Toronto, 1973.
- (19) Skell, P. S.; Traynham, J. G. *Acc. Chem. Res.* **1984**, 17, 160.
- (20) Work to be published from this laboratory.
- (21) Dantus, M.; Kim, S. B.; Williamson, J. C.; Zewail, A. H. *J. Phys. Chem.* **1994**, 98, 2782.
- (22) Williamson, J. C.; Zewail, A. H. *Chem. Phys. Lett.* **1993**, 209, 10.
- (23) Hargittai, I.; Hargittai, M. *Stereochemical Applications of Gas-Phase Electron Diffraction*; VCH: New York, 1988.
- (24) Yates, A. C. *Phys. Rev.* **1968**, 176, 173.
- (25) Bonham, R. A.; Schäfer, L. *Complex Scattering Factors for the Diffraction of Electrons by Gases. In International Tables For X-ray Crystallography*; Ibers, J. A., Hamilton, W. C., Eds.; Kynoch Press: Birmingham, 1974; Vol. IV.; p 176.
- (26) Sellers, H. L.; Schäfer, L.; Bonham, R. A. *J. Mol. Struct.* **1978**, 49, 125.
- (27) Bonham, R. A.; Bartell, L. S. *J. Chem. Phys.* **1959**, 31, 702.
- (28) Cao, J.; Ihee, H.; Zewail, A. H. *Chem. Phys. Lett.* **1998**, 290, 1.
- (29) Hedberg, L.; Mills, I. M. *J. Mol. Spectrosc.* **1993**, 160, 117.
- (30) Taylor, J. R. *An Introduction to Error Analysis: the Study of Uncertainties in Physical Measurements*; The University Science Book: Mill Valley, CA, 1982.
- (31) Thomassen, H.; Samdal, S.; Hedberg, K. *J. Am. Chem. Soc.* **1992**, 114, 2810.
- (32) Ihee, H.; J., K.; Goddard III, W. A.; Zewail, A. H. *J. Phys. Chem. A* **2001**, 105, 3623.
- (33) Bernardi, F.; Bottoni, A.; Fossey, J.; Sorba, J. *J. Mol. Struct.* **1985**, 119, 231.
- (34) Carlos, J. L.; Karl, R. R. J.; Bauer, S. H. *J. Chem. Soc., Faraday Trans. 2* **1973**, 70, 177.
- (35) Becke, A. D. *Phys. Rev. A* **1988**, 38, 3098.
- (36) Perdew, J. P.; Chevary, J. A.; Vosko, S. H.; Jackson, K. A.; Pederson, M. R.; Singh, D. J.; Fiolhais, C. *Phys. Rev. B* **1992**, 46, 6671.
- (37) Engels, B.; Peyerimhoff, S. D. *J. Mol. Struct.* **1986**, 138, 59.
- (38) Lobastov, V. A.; Ewbank, J. D.; Schäfer, L.; Ischenko, A. A. *Rev. Sci. Instrum.* **1998**, 69, 2633.